

Supporting information

An exploration of the compositional space for mixed lead halogen perovskites for high efficiency solar cells

T. Jesper Jacobsson^{1*}, Juan Pablo Correa Baena¹, Meysam Pazoki², Michael Saliba³, Kurt Schenk⁴, Michael Grätzel³, and Anders Hagfeldt^{*1,2}

1) Laboratory for Photomolecular Science, Institute of Chemical Sciences and Engineering, École Polytechnique Fédérale de Lausanne, CH-1015-Lausanne, Switzerland

2) Department of Chemistry - Ångström Laboratory, Uppsala University, Box 538, 75121 Uppsala, Sweden

3) Laboratory of Photonics and Interfaces, Institute of Chemical Sciences and Engineering, École Polytechnique Fédérale de Lausanne, CH-1015-Lausanne, Switzerland

4) École Polytechnique Fédérale de Lausanne, CH-1015-Lausanne, Switzerland

Jacobsson.jesper.work@gmail.com

+46 70 5745116

Anders.hagfeldt@epfl.ch

+41 (0)21 693 53 08

Experimental methods

In table S.1.a-f the concentration of the all relevant compounds are given for all 49 precursor solutions. A key between perovskite composition and sample number is given in table 1 in the main article, but is for convenience reproduced here in table S.2

Table S.1.a-f. Concentration of the precursors used in the different samples. The positions in the tables correspond to the same positions in table 1 giving the sample number and sample composition.

| | | [PbI ₂] (mol/dm ³) | | | | | | | | | [PbBr ₂] (mol/dm ³) | | | | | | |
|-----|--|--|------|------|------|------|------|---|-----|--|---|------|------|------|------|------|------|
| (a) | | 1 | 2 | 3 | 4 | 5 | 6 | 7 | (b) | | 1 | 2 | 3 | 4 | 5 | 6 | 7 |
| 1 | | 1.25 | 1.04 | 0.83 | 0.63 | 0.42 | 0.21 | 0 | 1 | | 0 | 0.21 | 0.42 | 0.63 | 0.83 | 1.04 | 1.25 |
| 2 | | 1.25 | 1.04 | 0.83 | 0.63 | 0.42 | 0.21 | 0 | 2 | | 0 | 0.21 | 0.42 | 0.63 | 0.83 | 1.04 | 1.25 |
| 3 | | 1.25 | 1.04 | 0.83 | 0.63 | 0.42 | 0.21 | 0 | 3 | | 0 | 0.21 | 0.42 | 0.63 | 0.83 | 1.04 | 1.25 |
| 4 | | 1.25 | 1.04 | 0.83 | 0.63 | 0.42 | 0.21 | 0 | 4 | | 0 | 0.21 | 0.42 | 0.63 | 0.83 | 1.04 | 1.25 |
| 5 | | 1.25 | 1.04 | 0.83 | 0.63 | 0.42 | 0.21 | 0 | 5 | | 0 | 0.21 | 0.42 | 0.63 | 0.83 | 1.04 | 1.25 |
| 6 | | 1.25 | 1.04 | 0.83 | 0.63 | 0.42 | 0.21 | 0 | 6 | | 0 | 0.21 | 0.42 | 0.63 | 0.83 | 1.04 | 1.25 |
| 7 | | 1.25 | 1.04 | 0.83 | 0.63 | 0.42 | 0.21 | 0 | 7 | | 0 | 0.21 | 0.42 | 0.63 | 0.83 | 1.04 | 1.25 |

| | | [FAI] (mol/dm ³) | | | | | | | | | [FABr] (mol/dm ³) | | | | | | |
|-----|--|------------------------------|------|------|------|------|------|---|-----|--|-------------------------------|------|------|------|------|------|------|
| (c) | | 1 | 2 | 3 | 4 | 5 | 6 | 7 | (d) | | 1 | 2 | 3 | 4 | 5 | 6 | 7 |
| 1 | | 1.14 | 0.95 | 0.76 | 0.57 | 0.38 | 0.19 | 0 | 1 | | 0 | 0.19 | 0.38 | 0.57 | 0.76 | 0.95 | 1.14 |
| 2 | | 0.95 | 0.79 | 0.63 | 0.47 | 0.32 | 0.16 | 0 | 2 | | 0 | 0.16 | 0.32 | 0.47 | 0.63 | 0.79 | 0.95 |
| 3 | | 0.76 | 0.63 | 0.51 | 0.38 | 0.25 | 0.13 | 0 | 3 | | 0 | 0.13 | 0.25 | 0.38 | 0.51 | 0.63 | 0.76 |
| 4 | | 0.57 | 0.47 | 0.38 | 0.28 | 0.19 | 0.09 | 0 | 4 | | 0 | 0.09 | 0.19 | 0.28 | 0.38 | 0.47 | 0.57 |
| 5 | | 0.38 | 0.32 | 0.25 | 0.19 | 0.13 | 0.06 | 0 | 5 | | 0 | 0.06 | 0.13 | 0.19 | 0.25 | 0.32 | 0.38 |
| 6 | | 0.19 | 0.16 | 0.13 | 0.09 | 0.06 | 0.03 | 0 | 6 | | 0 | 0.03 | 0.06 | 0.09 | 0.13 | 0.16 | 0.19 |
| 7 | | 0 | 0 | 0 | 0 | 0 | 0 | 0 | 7 | | 0 | 0 | 0 | 0 | 0 | 0 | 0 |

| | | [MAI] (mol/dm ³) | | | | | | | | | [MABr] (mol/dm ³) | | | | | | |
|-----|--|------------------------------|------|------|------|------|------|---|-----|--|-------------------------------|------|------|------|------|------|------|
| (e) | | 1 | 2 | 3 | 4 | 5 | 6 | 7 | (f) | | 1 | 2 | 3 | 4 | 5 | 6 | 7 |
| 1 | | 0 | 0 | 0 | 0 | 0 | 0 | 0 | 1 | | 0 | 0 | 0 | 0 | 0 | 0 | 0 |
| 2 | | 0.19 | 0.16 | 0.13 | 0.09 | 0.06 | 0.03 | 0 | 2 | | 0 | 0.03 | 0.06 | 0.09 | 0.13 | 0.16 | 0.19 |
| 3 | | 0.38 | 0.32 | 0.25 | 0.19 | 0.13 | 0.06 | 0 | 3 | | 0 | 0.06 | 0.13 | 0.19 | 0.25 | 0.32 | 0.38 |
| 4 | | 0.57 | 0.47 | 0.38 | 0.28 | 0.19 | 0.09 | 0 | 4 | | 0 | 0.09 | 0.19 | 0.28 | 0.38 | 0.47 | 0.57 |
| 5 | | 0.76 | 0.63 | 0.51 | 0.38 | 0.25 | 0.13 | 0 | 5 | | 0 | 0.13 | 0.25 | 0.38 | 0.51 | 0.63 | 0.76 |
| 6 | | 0.95 | 0.79 | 0.63 | 0.47 | 0.32 | 0.16 | 0 | 6 | | 0 | 0.16 | 0.32 | 0.47 | 0.63 | 0.79 | 0.95 |
| 7 | | 1.14 | 0.95 | 0.76 | 0.57 | 0.38 | 0.19 | 0 | 7 | | 0 | 0.19 | 0.38 | 0.57 | 0.76 | 0.95 | 1.14 |

Table S.2. Key between intended perovskite composition and sample number

| Pb | I ₃ | Br _{0.5} I _{2.5} | Br ₁ I ₂ | Br _{1.5} I _{1.5} | Br ₂ I ₁ | Br _{2.5} I _{0.5} | Br ₃ |
|-------------------------------------|----------------|------------------------------------|--------------------------------|------------------------------------|--------------------------------|------------------------------------|-----------------|
| FA | 1 | 2 | 3 | 4 | 5 | 6 | 7 |
| FA _{5/6} MA _{1/6} | 8 | 9 | 10 | 11 | 12 | 13 | 14 |
| FA _{4/6} MA _{2/6} | 15 | 16 | 17 | 18 | 19 | 20 | 21 |
| FA _{3/6} MA _{3/6} | 22 | 23 | 24 | 25 | 26 | 27 | 28 |
| FA _{2/6} MA _{4/6} | 29 | 30 | 31 | 32 | 33 | 34 | 35 |
| FA _{1/6} MA _{5/6} | 36 | 37 | 38 | 39 | 40 | 41 | 42 |
| MA | 43 | 44 | 45 | 46 | 47 | 48 | 49 |

Theory

Crystallographic properties

Perovskites is a class of compounds with the formula ABC_3 sharing both crystal structure and name with CaTiO_3 . The perovskites of primary interest for photovoltaic applications are organic lead halogen perovskites, where A is an organic ion, B is lead and C is a halogen. The basic structural motives are corner sharing lead-halogen octahedra, with the organic ion having a 12-fold symmetry occupying the cuboctahedral voids between the lead-halogen octahedra. This is illustrated in figure S.2a.c.

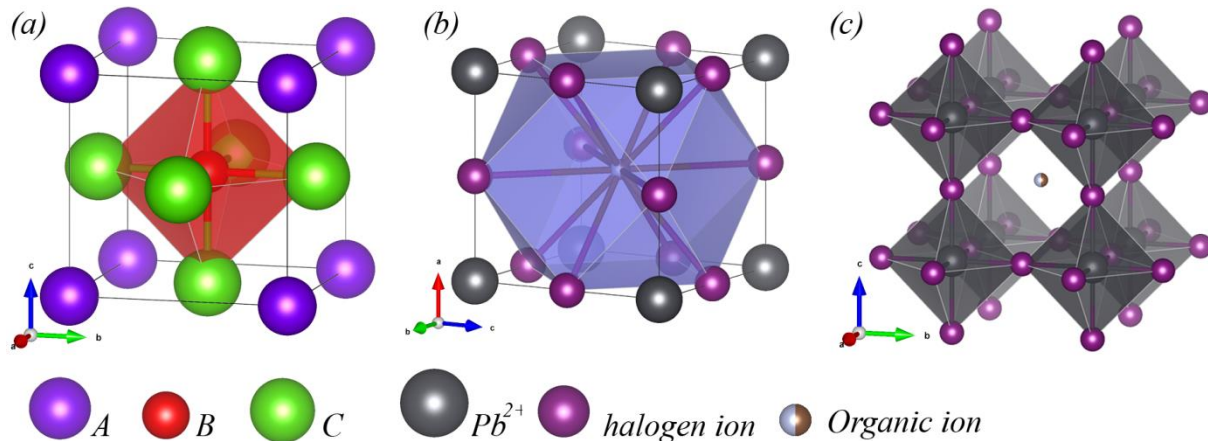


Figure S.2. (a) Unit cell of an idealized cubic methyl ammonium lead iodide perovskite. (b) The same structure as in *a* but illustrating the six fold coordination of Pb^{2+} and the corner sharing of the PbI_6 octahedra. (c) Same structure as in *b* but instead focusing on the connectivity between the PbI_6 octahedra. The structures are drawn in Vestas¹

Central for the structure of perovskites is the tolerance factor, t , which was introduced by Goldschmidt in the 1920's². The tolerance factor relates to the structure to the ionic radius according to eqn. S.1, where r_A , r_B , r_C , are the ionic radius of the A , B , and C ions, respectively.

$$t = \frac{r_A + r_C}{\sqrt{2}(r_B + r_C)} \quad (\text{s.1})$$

For a tolerance factor of one, the structure has an ideal cubic structure as the one in figure 2. Cubic structures at room temperature are generally found for tolerance factors between 0.9 and 1. For smaller tolerance factors, between 0.7 and 0.9, orthorhombic, rhombohedral or tetragonal structures are favoured. The ionic radius is 0.132 nm for Pb^{2+} , 0.206 nm for I^- and 0.18 nm for CH_3NH_3^+ ³. That gives a tolerance factor of 0.81 for MAPbI_3 , which is consistent with the tetragonal structure found experimentally for MAPbI_3 ^{4,5}. The bromide ion is slightly smaller (0.182 nm) than the iodide ion, but the tolerance factor is only increased to 0.82. Based on similarity of the tolerance factors, it would be reasonable to assume a tetragonal crystal structure also for MAPbBr_3 . Single crystal data for MAPbBr_3 does, however, indicate that a cubic structure is favoured⁵⁻⁷.

The formamidinium ion is slightly larger than the methyl ammonium ion which will increase the tolerance factor, favouring a cubic structure for the formamidinium rich compositions. FAPbI_3 is also found in a cubic perovskite phase⁸ or a singly distorted pseudo-cubic trigonal phase^{9,10} but has also been reported to form a tetragonal structure^{11,12}. A problem with FAPbI_3 is the instability of the perovskite phase which is not thermodynamically stable at room temperature and is observed to transform into a hexagonal yellow polymorph^{10,13}. Less work have been conducted on FAPbBr_3 but it has been reported to form a cubic phase at room temperature¹⁴.

Tetragonal perovskite structures have a tendency to transform into a cubic phase at elevated temperatures and for MAPbI₃ that is known to happen at 54°C¹⁵. That is potentially a problem as it is well within the temperature range a solar cell will experience at outdoor conditions. A composition that forms a cubic structure at normal ambient temperature may therefore have a technological advantage. If the corner compounds in the compositional matrix in figure 1 have different crystal symmetries, there will by necessity be a dividing line between those somewhere in the matrix, which is explored in the experimental section.

To facilitate the evaluation and interpretation of experimental XRD-data, we have simulated a theoretical powder diffractogram for the tetragonal phase of MAPbI₃. The data used in the simulation is based on single crystal data from Dang et al.⁴ and is given in figure 3. MAPbI₃ transforms to a cubic phase at 54°C and a simulation for the cubic phase, based on cell parameters from Constantinou et al.¹³, is also given in figure 3. Even if high temperature data is not sampled in this work, the cubic phase of MAPbI₃ is a suitable baseline for comparisons with the experimental data of the mixed perovskites of which some could be expected to be cubic. The indexation of the major peaks is given in the figure and the full indexation of all peaks is found in one of our previous papers¹⁵. The difference between the tetragonal and the cubic structure is seen as a few extra peaks for the tetragonal phase, like the (121) peak, and a split of some of the peaks seen as single peaks in the cubic structure. The differences are, however, not very large and for polycrystalline films, good XRD-data on samples without too strong texturation is required for it to be apparent.

Based on ion size it is reasonable to assume a slight decrease in the cell parameters as iodine is replaced by bromide and a corresponding increase when methyl ammonium is replaced by formamidinium. That will be observed as a shift in the positions of the XRD-reflections.

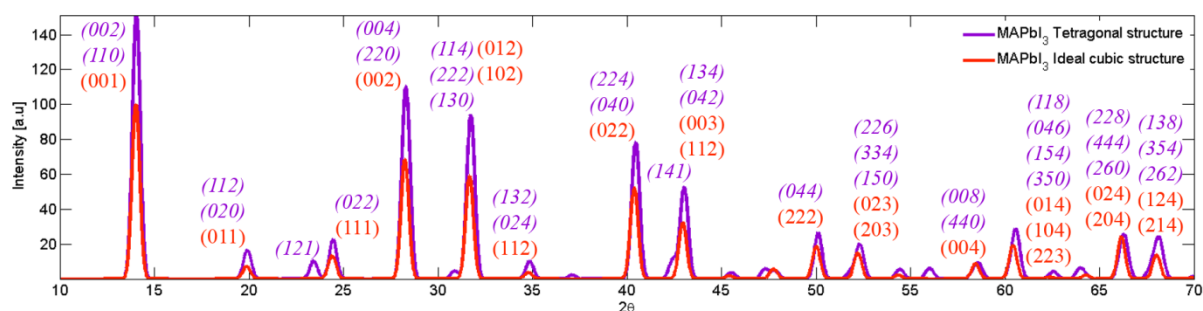


Figure S.3. Simulated XRD patterns for the cubic and the tetragonal phase of CH₃NH₃PbI₃. The indexation for the major peaks is given in the figure. Italic entries represent the tetragonal phase and regular entries represent the cubic phase.

The perovskites are made from precursor solutions of PbI₂ and PbBr₂. Those have different crystal structures which could affect the crystallization dynamics. PbI₂ has a layered structure where the layers are composed of edge sharing PbI₆ octahedra, whereas PbBr₂ form an interlinked network of edge and corner sharing PbBr₆ octahedra.

In figure S.4.a, the crystal structure of PbI₂ is given and the corresponding diffractogram is given in figure S.5.a. The basic structural theme in PbI₂ is edge sharing PbI₆ octahedra that are stacked in layers. PbBr₂ is not as well investigated as the iodide salt and less data is available. The stable phase calculated according to materials project¹⁶ is given in figure S.4.b and is composed of edge and corner sharing PbBr₆ octahedra. In figure S.5.b a diffractogram is given for a film of PbBr₂ produced from spin coating from a solution of PbBr₂ in DMF:DMSO (4:1). The diffractogram for PbBr₂ is distinctly different from the PbI₂ diffractogram indicating that the structures are different. It is at the same time a only a moderately good fit that not is excellent with respect to the theoretical spectra from the structure from the materials project¹⁶, leaving us with some degree of uncertainty over the precise structure of the PbBr₂ precursor used in the synthesis.

A likely mechanistic pathway for the formation of iodide perovskites is intercalation of the organic ions into the PbI_2 structure, as illustrated in figure S.4.c. That view is supported by the considerably lower solubility of the PbI_2 salt compared to the organic salts and by the success of the two-step synthesis procedure where PbI_2 is deposited first and then exposed to MAI^{17} .

No mechanism for the formation of the bromide perovskites are here proposed, but given the non-layered structure it is reasonable to assume that it may be somewhat modified.

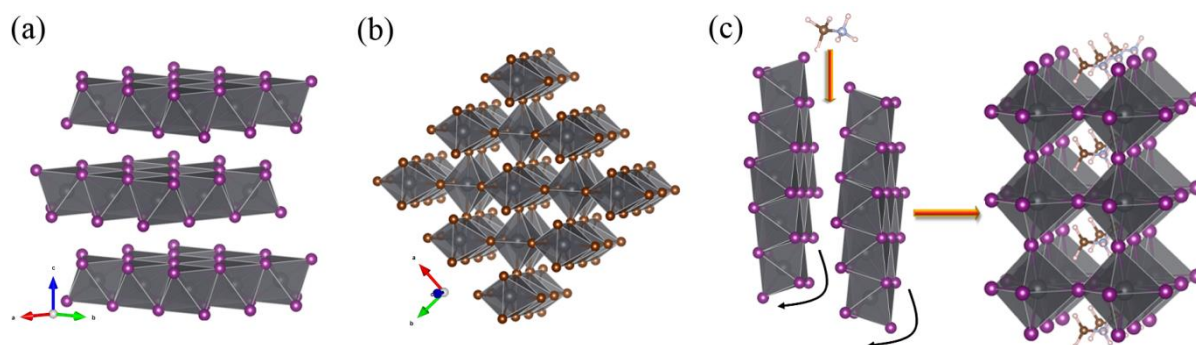


Figure S.4. (a) The layered crystal structure of PbI_2 . (b) The distinctly non-layered crystal structure of PbBr_2 . (c) Part of possible mechanistic pathway for the formation of MAPbI_3 caused by intercalation of the inorganic ions into the layered structure of PbI_2 .

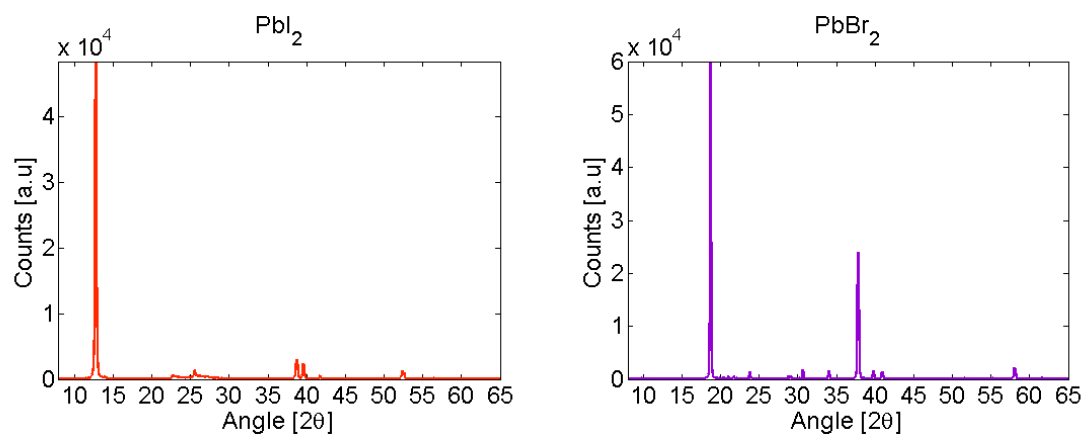


Figure S.5. (a) XRD diffractogram of PbI_2 . (b) XRD diffractogram of PbBr_2

Tandem applications

Perovskite cells have now been produced, at least in lab-scale, with efficiencies exceeding 20 % which makes them of potential commercial interest. However, entering the market place as a standalone technology may prove challenging and is probably not the first application that will go commercial^{18,19}. A second, somewhat more likely pathway would be to use the perovskites as an add-on to existing solar cell technologies, i.e. silicon, CIGS or CdTe. The function of the perovskite would be as a top cell in a tandem architecture. There are several benefits with such an approach. To act as a standalone technology, the perovskite would need to match silicon, which is hard given the position silicon have in terms of efficiency, large scale production, installation etc. In a tandem architecture, some demands are reduced and by combining a decent silicon cell with a decent perovskite cell, something that performs better than top quality silicon is achievable^{20,21}. As one of the main driver for overall cost reduction in silicon solar cells is to increase cell efficiency, such a solution gives a favorable economics to the problem. At the same time, the perovskite could ride upon the established silicon technology and thereby prove itself for further applications.

The tandem architecture puts a number of constraints upon the materials used as the number of low recombination interfaces increases and the current from the two photo-absorbers need to match. The latter requirement provides constraints in the band gap of the two cells, which make it highly desirable with materials where the band gap can be tuned to match the other photo-absorber. While evaluating the expectations that could be set upon an efficient tandem system, a good limiting case is the optical limit of the current density under ideal conditions. The details and derivations is given in the supporting information. The results in terms of the theoretical maximum current obtainable from a two band gap tandem system, given as a function of the band gap of the top and bottom cells under AM 1.5 illumination, is given in figure 5.a. Some of the most relevant vertical paths in figure 4.a is given in figure 5.b where the optical limit of the photocurrent is plotted as a function of the band gap for the top cell, which could be a perovskite, against the band gap of some possible bottom cells. It is apparent that the efficiency that could be obtained by the tandem system, with a given bottom cell, drops rather fast when the band gap of the top cell deviates from the ideal match. This is entirely symmetrical for the band gap of the bottom cell if the band gap of the top cell is fixed. This analysis clearly illustrates the importance of being able to tune at least one of the band gaps while designing tandem cells, as is the case for the perovskites. More important than the current is the output power, which depends on a fairly long range of parameters. If reasonable parameters are chosen, an estimation of what can be obtained from a good tandem device is given. The details are given below and a graphical illustration is given in figure 5.c, which can guide the design of a perovskite based tandem system.

Evaluation of tandem cells

For a single band gap solar cell, the photocurrent density is given by eqn. S.2, where J_{ph} is the photocurrent density, E is the excitation spectra, or photon flux, which in the analysis is taken as the AM 1.5 spectrum, λ is the wavelength, EQE is the external quantum efficiency, and the integration is carried out over the entire wavelength range provided by E .

$$J_{ph} = \int_0^{\infty} E(\lambda)EQE(\lambda)d\lambda \quad (S.2)$$

The theoretical upper bound to the photocurrent density in a single band gap cell is given by eqn. S.3, where the quantum efficiency is assumed to be unity over the entire spectrum, and the integration limits are exchanged to zero and the wavelength corresponding to the band gap energy. The same result will be obtained if the integration limits in eqn. S.2 is kept but EQE is replaced by a step function that has the value of one for energies above the band gap and zero at lower energies.

$$J_{ph \max} = \int_{\lambda_1}^{\lambda_2} E(\lambda)d\lambda, \quad \lambda_1 = 0, \quad \lambda_2 = \frac{hc}{E_g} \quad (S.3)$$

The true measure of interest is not the photocurrent but the power delivered by the device, which is the product of the photocurrent and the photo-voltage, V_{ph} . The photo-voltage under operational conditions is expressed as the product between the open circuit voltage, V_{oc} , and an voltage efficiency factor $\eta_{V_{oc}}$, which in turn depends on the fill factor, FF , the short circuit current, J_{sc} and the current density in the working point, J_{mp} , as in eqn. S.4, where the fill factor is a measure of how ideally the system behaves from a photovoltaic perspective.

$$V_{ph} = V_{oc} \cdot \eta_{V_{oc}} = V_{oc} \cdot FF \cdot \frac{J_{sc}}{J_{mp}} \quad (S.4)$$

The open circuit voltage can be seen as the difference between the quasi Fermi levels for the electrons and holes under illumination and is a measure of the energy difference between the photo-generated electron and the hole. This energy will be smaller than the band gap energy by an amount η_{sep} , which can be seen as the energy penalty for withholding the electric field separating the photocarriers. A formulation of this loss, (η_{sep}), was derived by Shockley and Queisser²² and can by neglecting higher order terms be written as eqn S.5²³

$$V_{oc} = E_g - \eta_{sep} = E_g - k_B T \ln \left[\frac{8\pi(k_B T)^2}{c^2 h^3} \frac{n^2 E_g}{j_{gen}} \alpha L \Phi_{rec} \right] \quad (S.5)$$

where E_g is the band gap, k_B is the Boltzmann's constant, T is the temperature, h Planck's constant, c is the speed of light in vacuum, n is the refractive index, j_{gen} is the rate of photon absorption in the AM1.5 spectra, f_{rec} is the ratio between the non-radiative and radiative recombination rates, a is the absorption coefficient, and L is the minority carrier diffusion length which should be replaced with the material thickness, d , if $d < L$.

This energy penalty, η_{sep} , depends on both the material and on material purity. Some typical values for state-of-the-art materials in solar cells are: 0.36 eV in silicon, 0.3 eV in GaAs, 0.4 eV in InP, 0.45 eV in CIGS, 0.6 eV in CdTe, and 0.61 eV in amorphous silicon. That correlates reasonably well with the theoretical assumptions in eqn S.4. For the perovskites, values below 0.4

are commonly observed which is in line with some of the best solar cell materials. The power output for a single band gap cell can thus be expressed as in eqn. S.6.

$$P = V_{ph} \cdot J_{ph} = \eta_{V_{oc}} \cdot (E_g - \eta_{sep}) \cdot \int_0^{hc/E_g} E(\lambda) \cdot EQE(\lambda) d\lambda \quad (S.6)$$

Using some prototypical values of the parameters in eqn. S.6 ($\eta_{V_{oc}} = 0.85$, $\eta_{sep} = 0.4$ and $EQE = 0.9$) the expected power output for a good solar cell are plotted as a function of band gap in figure S.6.a. This gives the optimal value for a single band gap device somewhere between 1.1 to 1.4 eV. That is fairly close to silicon which further illustrates the problem perovskites will have in competing with silicon by itself, talking in favor for a tandem concept.

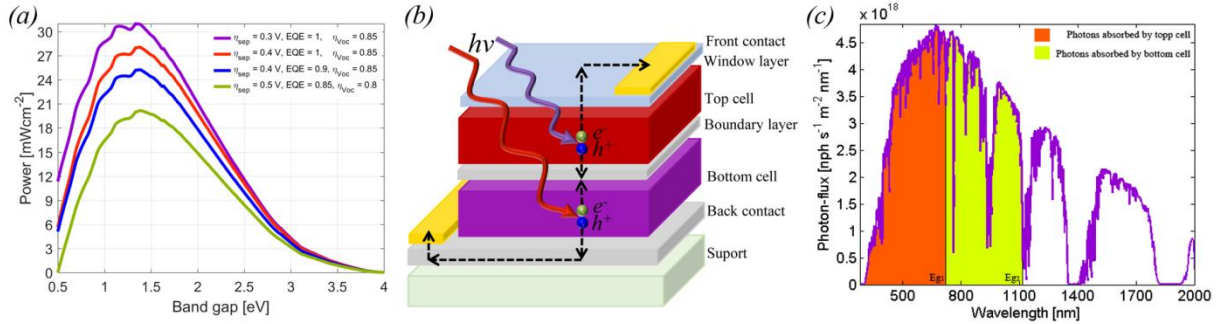


Figure S.6. (a) Expected power output from a good solar cell as a function of band gap for a few different set of assumptions. (b) Schematic structure of a tandem cell. (c) An illustration of proper current matching in a tandem cell based on the photon-flux in the solar AM 1.5 spectrum.

In a tandem cell, two photo-absorbers with different band gaps are stacked on top of each other as in figure S.6.b. In this configuration, the two cells must share the photons in the solar spectra between them, as graphically illustrated in figure S.6.c, and for an efficient device they need to share equally.

The photocurrent generated in the top cell, $J_{ph top}$, which have the higher band gap, is given by eqn. S.7, where E_{g1} is the band gap of the top cell. The photocurrent of the bottom cell, $J_{ph bot}$, is given by eqn. S.8 where E_{g2} is the band gap of the bottom cell. The total current from the tandem cell will be the smallest of the currents of the two individual cells as expressed in eqn. S.9.

$$J_{ph top} = \int_0^{hc/E_{g1}} E_1(\lambda) EQE_1(\lambda) d\lambda \quad (S.7)$$

$$J_{ph bot} = \int_{hc/E_{g1}}^{hc/E_{g2}} E_2(\lambda) EQE_2(\lambda) d\lambda \quad (S.8)$$

$$J_{ph tot} = \min \{ J_{ph top}, J_{ph bot} \} \quad (S.9)$$

The ideal optical limit in terms of photocurrent for a two cell tandem devices is given by assuming that $EQE_1 = EQE_2 = 1$, $E_1 = AM 1.5$, and that the top cell absorbs all light above the threshold, given by the band gap, but no light of lower energy. The last requirement is numerically obtained by either setting $E_1 = E_2$ using the integration limits in eqn. S.8, or by setting EQE_2 as a step function, or by setting all values of E_2 for energies higher than the band gap of the top cell to zero. An illustration of the results of these integrations is given in figure S.7.a. In figure S.7.b the optical limit of the photocurrent is plotted as a function of the band gap for the top cell, which could be a perovskite, against the band gap of some possible bottom cells.

One thing that is apparent is that the efficiency that could be obtained by the tandem system, with a given bottom cell, drops rather fast when the band gap of the top cell deviates from the ideal. This is of course entirely symmetrical for the band gap of the bottom cell if the band gap of the top cell is fixed. This analysis clearly illustrates the importance of being able to tune at least one of the band gaps while designing tandem cells.

The photo voltage, V_{ph} , for a tandem cell is given by the sum of the photo voltages of the two cells, V_{top} and V_{bot} , as in eqn. S.10, which in turn is given by eqn. S.4.

$$V_{ph} = V_{top} + V_{bot} \quad (S.10)$$

The output power of a tandem cell thus depends on a fairly long range of parameters as illustrated in eqn. S.11. If some reasonable parameters are assumed ($EQE_1 = EQE_2 = 0.9$, $\eta_{sep1} = \eta_{sep2} = 0.4$, $\eta_{Voc1} = \eta_{Voc2} = 0.8$) an estimation of what can be obtained from a good tandem device is given. This is presented in figure S.7.c, where the output power was divided with the power of the solar spectrum in order to get the efficiency.

$$P(E_{g1}, E_{g2}) = J_{ph\ tot}(E_{g1}, E_{g2}, EQE_1, EQE_2) \cdot V_{ph}(E_{g1}, E_{g2}, \eta_{sep1}, \eta_{sep2}, \eta_{Voc1}, \eta_{Voc2}) \quad (S.11)$$

$$P(E_{g1}, E_{g2}) \approx \min \left\{ \int_0^{hc/E_{g1}} AM_{1.5}(\lambda) \cdot 0.9 d\lambda, \int_{hc/E_{g1}}^{hc/E_{g2}} AM_{1.5}(\lambda) \cdot 0.9 d\lambda \right\} \cdot ((E_{g1} - 0.4) \cdot 0.8 + (E_{g2} - 0.4) \cdot 0.8) \quad (S.12)$$

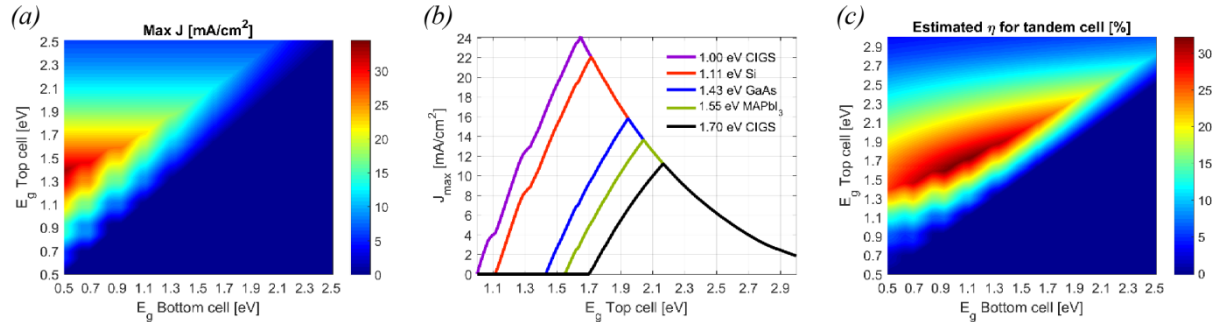


Figure S.7. (a) Ideal optical limit current limit in a tandem cell as a function of the band gaps of the top and bottom cell. (b) Optical current limit for a tandem cell as a function of the band gap of the top cell for a number of possible bottom cells. (c) Estimated top performance of a tandem cell as a function of the band gap for the top and bottom cells.

Complementary computational results

To investigate and predict the trend of possible band shifts in the mixed perovskites, periodic crystal calculations were performed on the four corner compounds: MAPbI₃, MAPbBr₃, FAPbI₃, and FAPbBr₃. From these calculations, the density of states, DOS, as well as the partial density of states, PDOS, for the metal cation, the halogen, and the organic cation were extracted. The results of these simulations are given in figure S8.a-h.

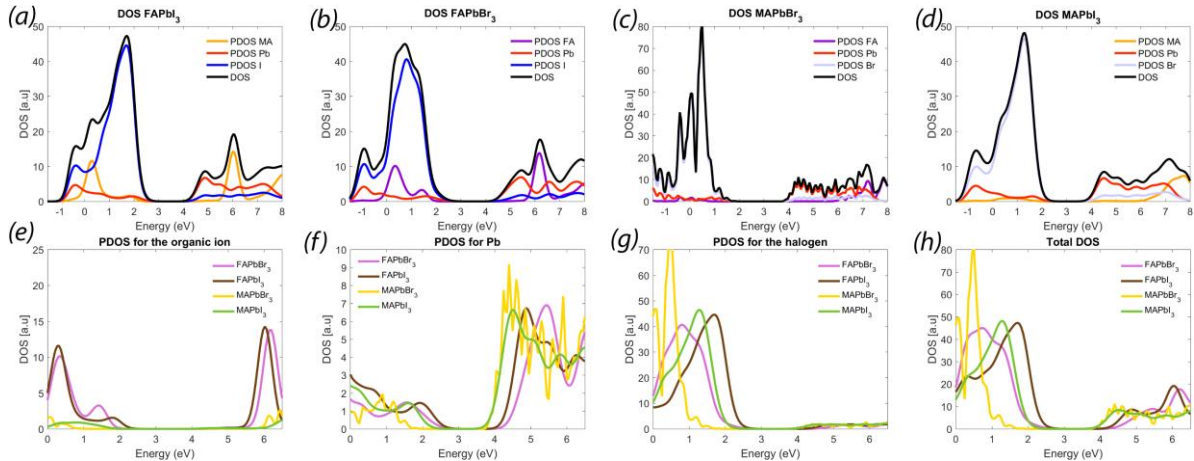


Figure S.8. (a) PDOS for FAPbI₃. (b) PDOS for FAPbBr₃. (c) PDOS for MAPbBr₃. (d) PDOS for MAPbI₃. (e) PDOS for the organic ions in the four corner compounds. (f) PDOS for the lead ion in the four corner compounds. (g) PDOS for the halogen in the four corner compounds. (h) DOS for the four corner compounds.

From the simulations, the band gaps of MAPbI₃, MAPbBr₃, FAPbI₃, and FAPbBr₃ were determined to 1.6, 2.3, 1.5 and 2.05 eV, respectively. There is some uncertainty to these numbers due to the well-known band gap problem associated with DFT calculations, but the values are fairly close to our experimental values. For MAPbI₃, MAPbBr₃, and FAPbI₃ they are within 50 meV from the experimental values, and for FAPbBr₃ the deviation is around 200 meV. This indicates that the error cancellation from the spin-orbit coupling and the scalar relativistic effects in lead is favorable in this case^{24,25}, rendering a reasonable trustworthiness for qualitative discussions based on the simulated data.

Lead is seen to be the main contributor of states close to the conduction band edge, whereas the halogen is the main contributor to states close to the valence band edge which is evident from the PDOS curves in figure 5.e-h. The organic ions do not contribute with any appreciable amount of states to the band edges and has thus no direct effect on the band gap. This is consistent with the experimental data where the halogen is observed to impact the optical behavior to a far greater extent than the organic ion. The organic ions could, however, have an indirect effect as they can shift the tilt of the lead halogen octahedra, which is a parameter known to affect the band gap²⁶⁻²⁹.

The tight binding approximation was used to interpret the band edge shifts between the different perovskites. In that framework the periodic energy level of the electrons is related to the molecular energy levels according to eqn. S.13. The position of the conduction band edge depends on the charge density overlap integrals, which in turn depends on the tilting angle of the lead-halogen octahedral, and we here observe a trend of the conduction band edge shift and the tilting angle. The position of the valence band edge is strongly affected by the electronegativity and the molecular levels of the halogen. In table S.3 the simulated tilting angles of the lead-halogen octahedra is given for the four corner compounds in the compositional matrix. The tilting correlates to some extent to the band gap.

$$\varepsilon(\mathbf{k}) - E_m = \frac{\int \Psi_m^*(r) \Delta u \Psi(r) dr}{\int \Psi_m^*(r) \Psi(r) dr} \quad (\text{S.12})$$

Table S.3. Tilting angles of the lead-halogen octaedra

| Tilting angle | MaPbI3 | FAPbI3 | MAPbBr3 | FaPbBr3 |
|---------------|--------|--------|---------|---------|
| Horizontal | 170° | 178° | 170° | 178° |
| Vertical | 154° | 170° | 174° | 176° |

Absorption data

In figure S.9 the full set of absorption figures is presented. The layout with respect to perovskite composition is the same as in figure 1 in the main article. In figure S.10 the absorption is compared for samples with the same MA/FA-ratio. The seven figures in S.10 correspond to the seven rows in figure S.9. In figure S.11 the corresponding figures for a fixed Br/I-ratio, corresponding to the columns in figure S.9, is given. In figure S.12 a photo of the full set of films is given.

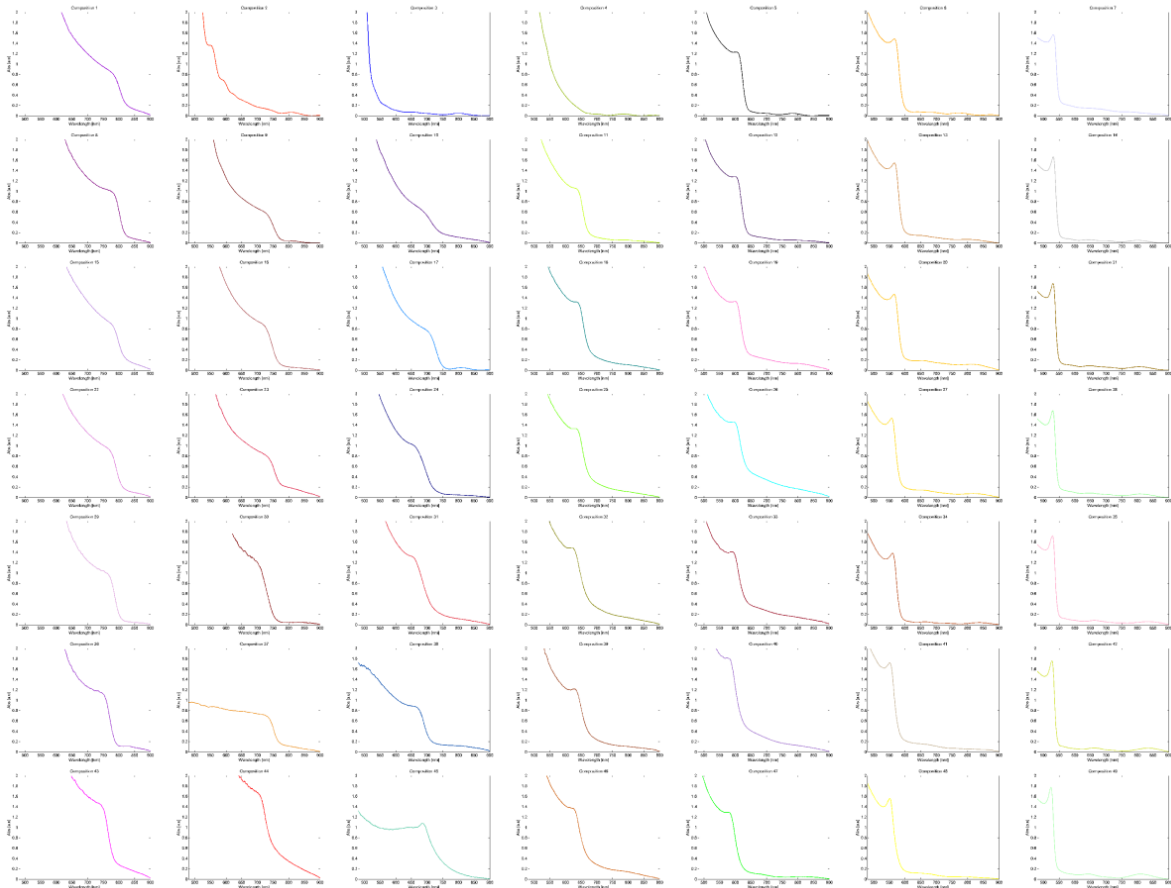


Figure S.9. Absorption against wavelength. The full set of absorption figures.

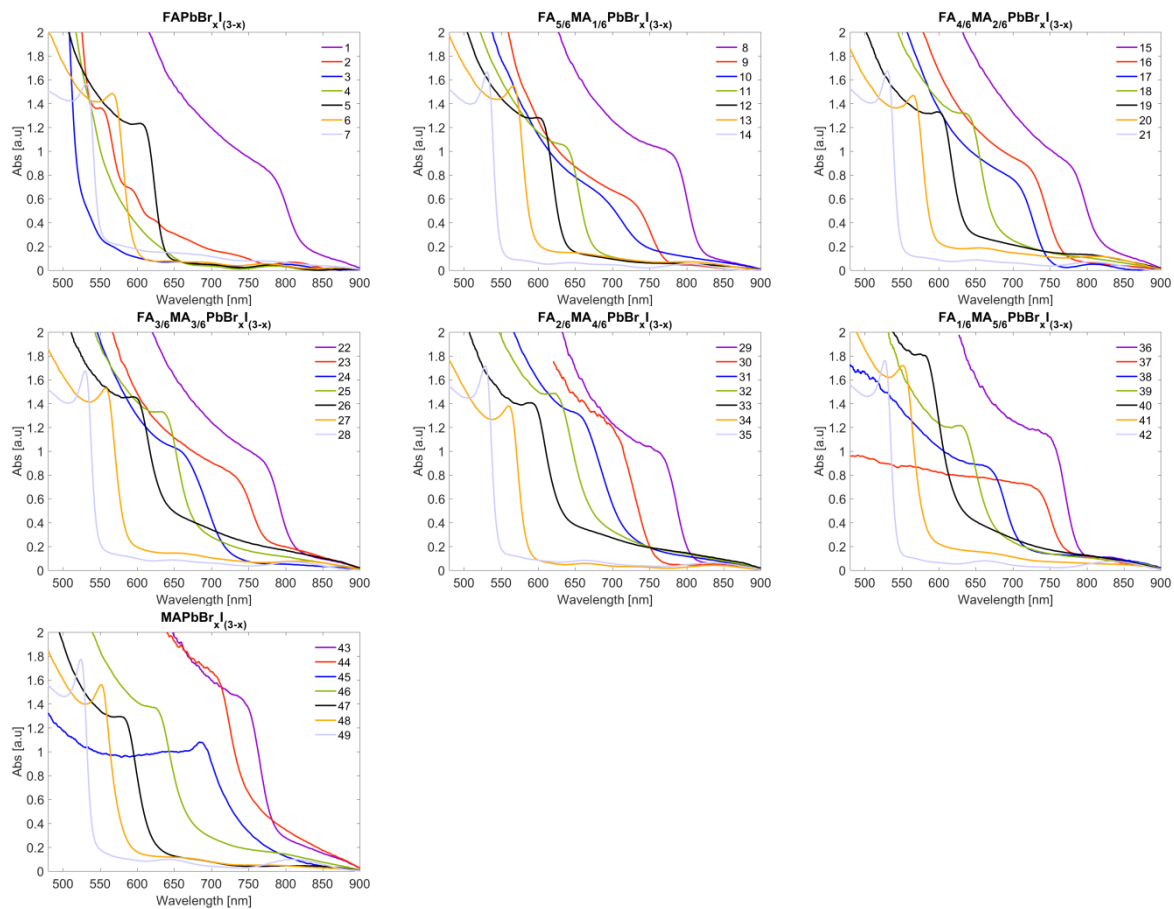


Figure S.10. Optical absorption as a function of wavelength. Each figure represent a fixed MA/FA-ratio and a changing Br/I-ratio.

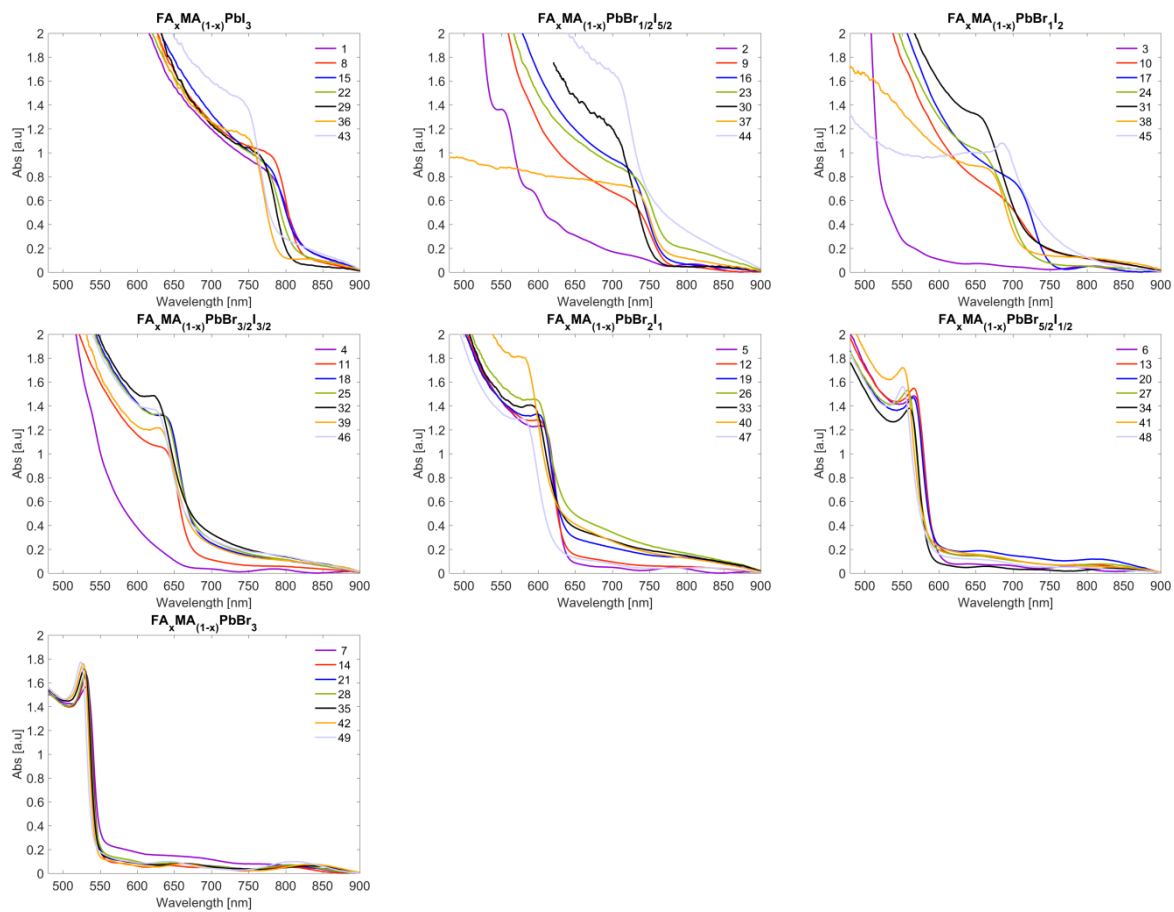


Figure S.11. Optical absorption as a function of wavelength. Each figure represent a fixed Br/I-ratio and a changing MA/FA-ratio.

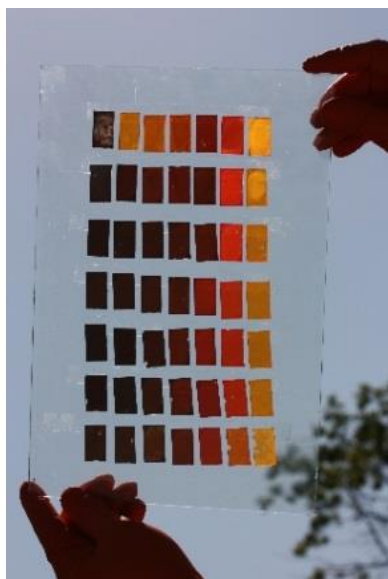


Figure S.12. A photo of the full set of perovskite films.

Band gap determinations

In figure S.13 the full set of figures used to extract the band gaps of the different perovskites is presented. The layout with respect to perovskite composition is the same as in figure 1 in the main article.

In eqn. S.14 a proposed functional form for how the band gap depends on composition is given. The motivation behind this functional form is elaborated in the main article. In eqn. S.14 the numbers fitted to the coefficients are explicitly given, and the confidence intervals by which they were determined are given in table S.4. An illustration of the goodness of fit between the experimental band gap data and the band gaps predicted from eqn. S.15 is given in figure S.14

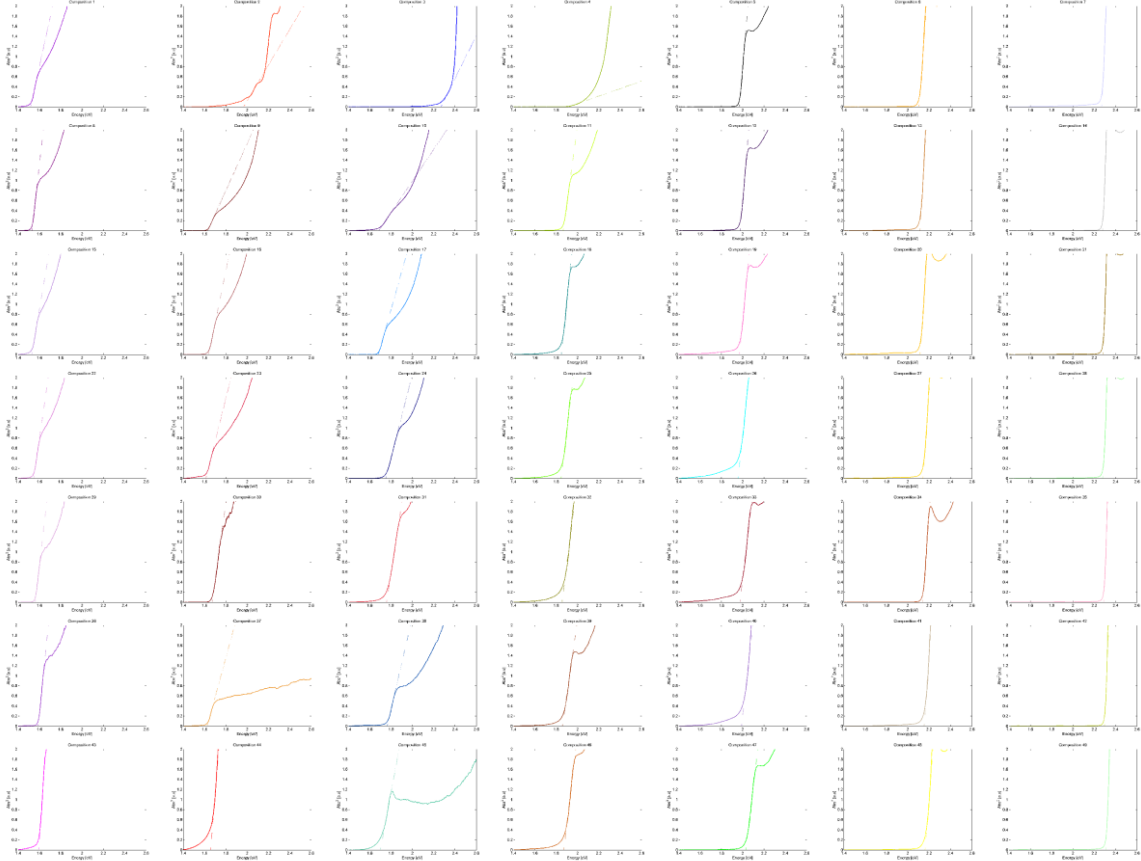


Figure S.13. The square of absorption against photon energy. The band gap is given as the intercept between the linear regions close to the absorption onset and the intercept. The figures are ordered in the same way as in figure 1 in the main article.

$$Eg(x, y) = C_1 + C_2 \cdot x + C_3 \cdot y + C_4 \cdot x^2 + C_5 \cdot x \cdot y \quad (\text{S.14})$$

$$Eg(x, y) = 1.58 + 0.436x - 0.0580y + 0.294x^2 + 0.0199x \cdot y \quad (\text{S.15})$$

$$x = \frac{[Br]}{[Br] + [I]}, y = \frac{[FA]}{[FA] + [MA]}$$

Table S.4. Values of the coefficients in eqn. (x) with 95% confidence bounds

| Coefficient | Value | Lower bound | Upper bound |
|----------------|---------|-------------|-------------|
| C ₁ | 1.579 | 1.56 | 1.60 |
| C ₂ | 0.436 | 0.366 | 0.506 |
| C ₃ | -0.0580 | -0.096 | -0.0200 |
| C ₄ | 0.294 | 0.232 | 0.357 |
| C ₅ | 0.0199 | -0.0433 | 0.0831 |

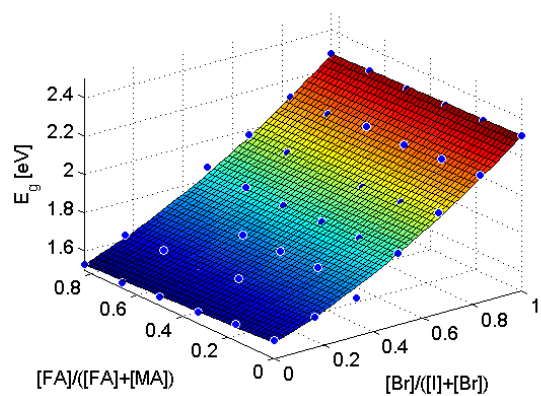


Figure S.14. Experimental band gaps compared to the ones given from the empirical relation in eqn. S.14

Photoluminescence data

In figure S.15 steady state photoluminescence as a function of wavelength is given together with absorption for all 49 different compositions. The wavelength corresponding to the band gap energy is marked by a vertical line. In figure S.16 bar graphs illustrating the peak positions for the primary and the secondary PL-peak is presented. In table S.4 the peak positions corresponding to the peaks in figure S.12.b is given. In figure S.17 the PL-spectra is compared for samples with the same MA/FA-ratio. The seven figure sin S.17 corresponds to the seven rows in figure S.15. In figure S.14 the corresponding figures for a fixed Br/I-ratio, corresponding to the columns in figure S.15, is given. In figure S.18 and S.19 the corresponding data is presented in un-normalized form.

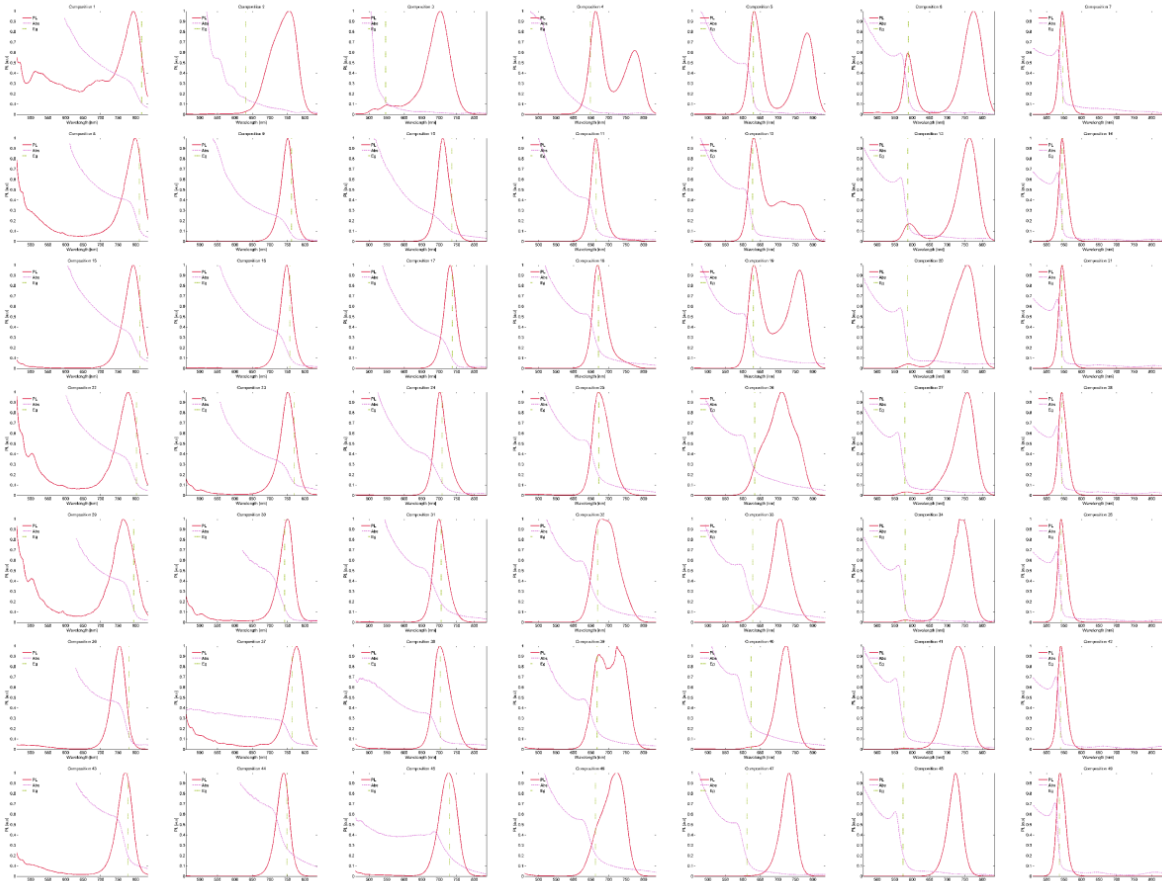


Figure S.15. Steady state photoluminescence as a function of wavelength for all 49 compositions. The layout of the sub panels are the same as in figure 1 in the main article.

Table S.5.a Primary PL peak position

| Pb | I_3 | $Br_{0.5}I_{2.5}$ | $Br_{1}I_2$ | $Br_{1.5}I_{1.5}$ | Br_2I_1 | $Br_{2.5}I_{0.5}$ | Br_3 |
|--------------------|-------|-------------------|-------------|-------------------|-----------|-------------------|--------|
| FA | 793 | 755 | 703 | 663 | 632 | 587 | 544 |
| $FA_{5/6}MA_{1/6}$ | 798 | 751 | 710 | 663 | 631 | 591 | 544 |
| $FA_{4/6}MA_{2/6}$ | 793 | 748 | 731 | 668 | 631 | 589 | 544 |
| $FA_{3/6}MA_{3/6}$ | 778 | 751 | 701 | 671 | 660 | 584 | 543 |
| $FA_{2/6}MA_{4/6}$ | 764 | 750 | 699 | 679 | 640 | 583 | 541 |
| $FA_{1/6}MA_{5/6}$ | 754 | 776 | 701 | 670 | 635 | 578 | 540 |
| MA | 770 | 739 | 726 | 670 | 731 | 723 | 538 |

Table S.5.b. Secondary PL peak position

| Pb | I_3 | $Br_{0.5}I_{2.5}$ | $Br_{1}I_2$ | $Br_{1.5}I_{1.5}$ | Br_2I_1 | $Br_{2.5}I_{0.5}$ | Br_3 |
|--------------------|-------|-------------------|-------------|-------------------|-----------|-------------------|--------|
| FA | 0 | 0 | 0 | 775 | 783 | 775 | 0 |
| $FA_{5/6}MA_{1/6}$ | 0 | 0 | 0 | 760 | 710 | 764 | 0 |
| $FA_{4/6}MA_{2/6}$ | 0 | 0 | 0 | 745 | 762 | 757 | 0 |
| $FA_{3/6}MA_{3/6}$ | 0 | 0 | 0 | 0 | 710 | 757 | 0 |
| $FA_{2/6}MA_{4/6}$ | 0 | 0 | 0 | 692 | 705 | 734 | 0 |
| $FA_{1/6}MA_{5/6}$ | 0 | 0 | 0 | 731 | 725 | 731 | 0 |
| MA | 0 | 0 | 0 | 723 | 0 | 0 | 0 |

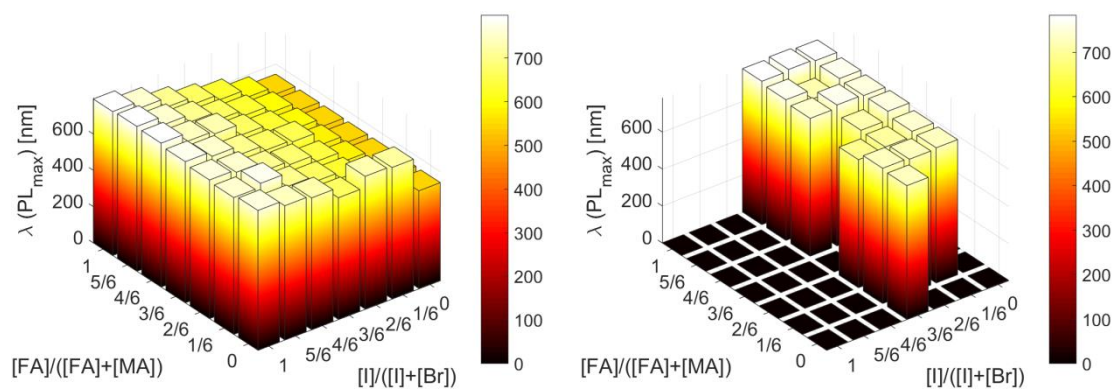


Figure S.16. (a) Position of the primary PL-peak corresponding to band gap recombination. (b) Position of the secondary peak corresponding to sub band gap recombination

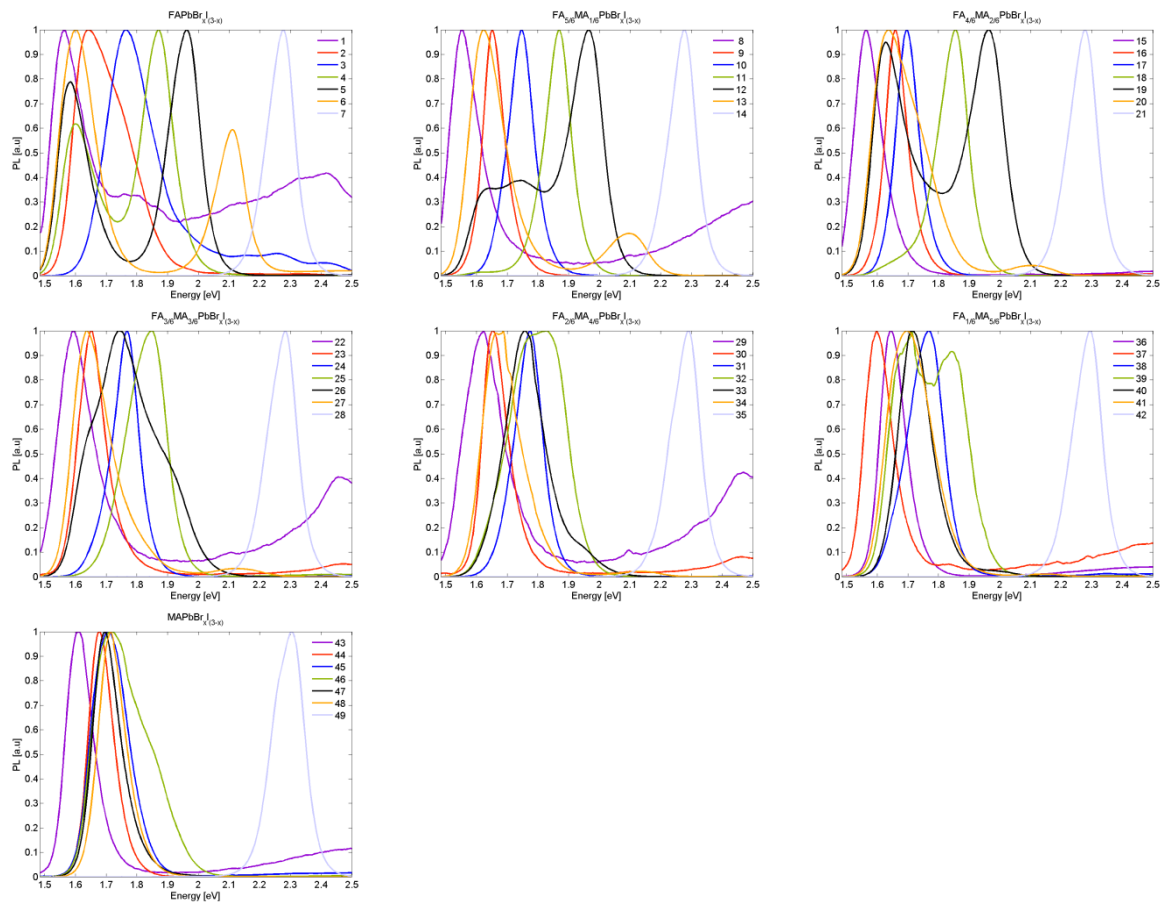


Figure S.17. Steady state photoluminescence against wavelength. Each figure represents a fixed MA/FA-ratio and a changing Br/I-ratio. Data is normalized.

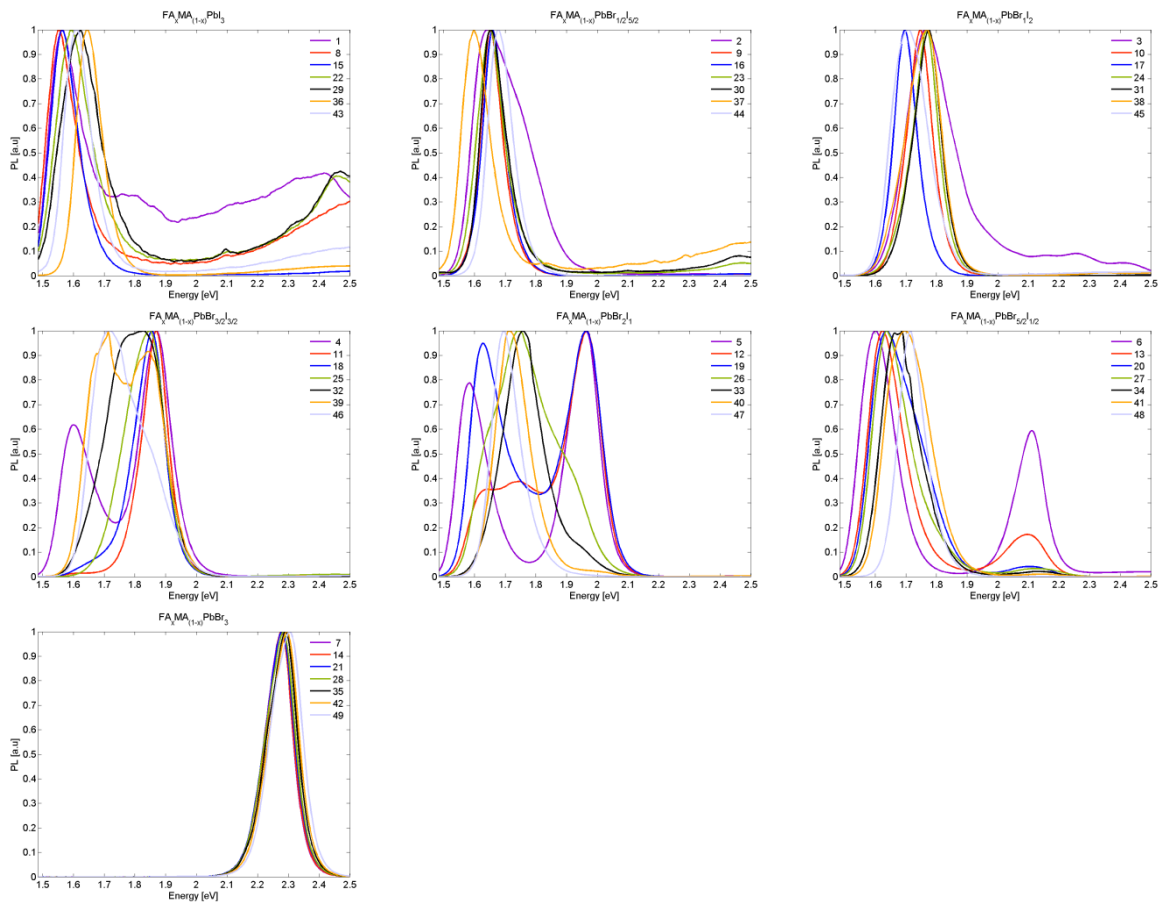


Figure S.18. Steady state photoluminescence against wavelength. Each figure represents a fixed Br/I -ration and a changing MA/FA-ratio. Data is normalized.

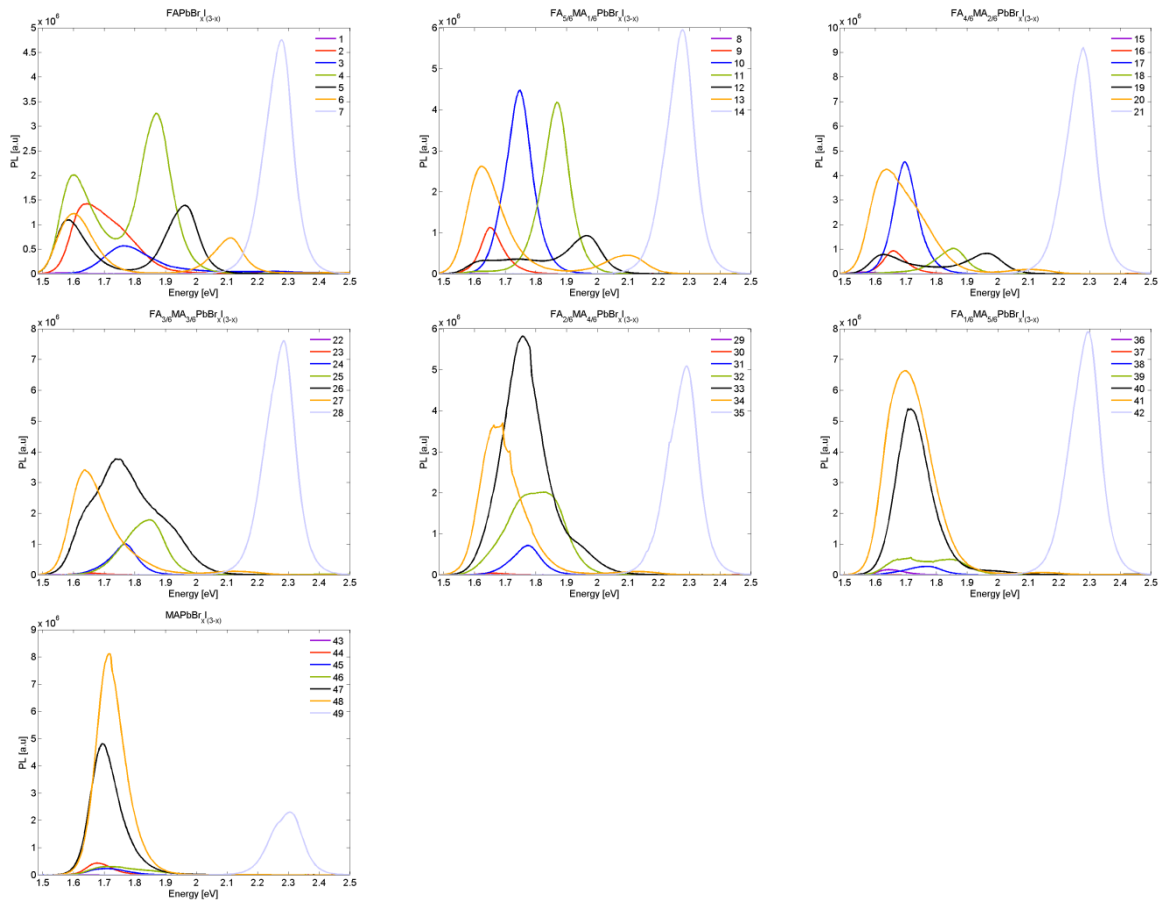


Figure S.19. Steady state photoluminescence against wavelength. Each figure represents a fixed MA/FA-ratio and a changing Br/I-ratio. Data is not normalized.

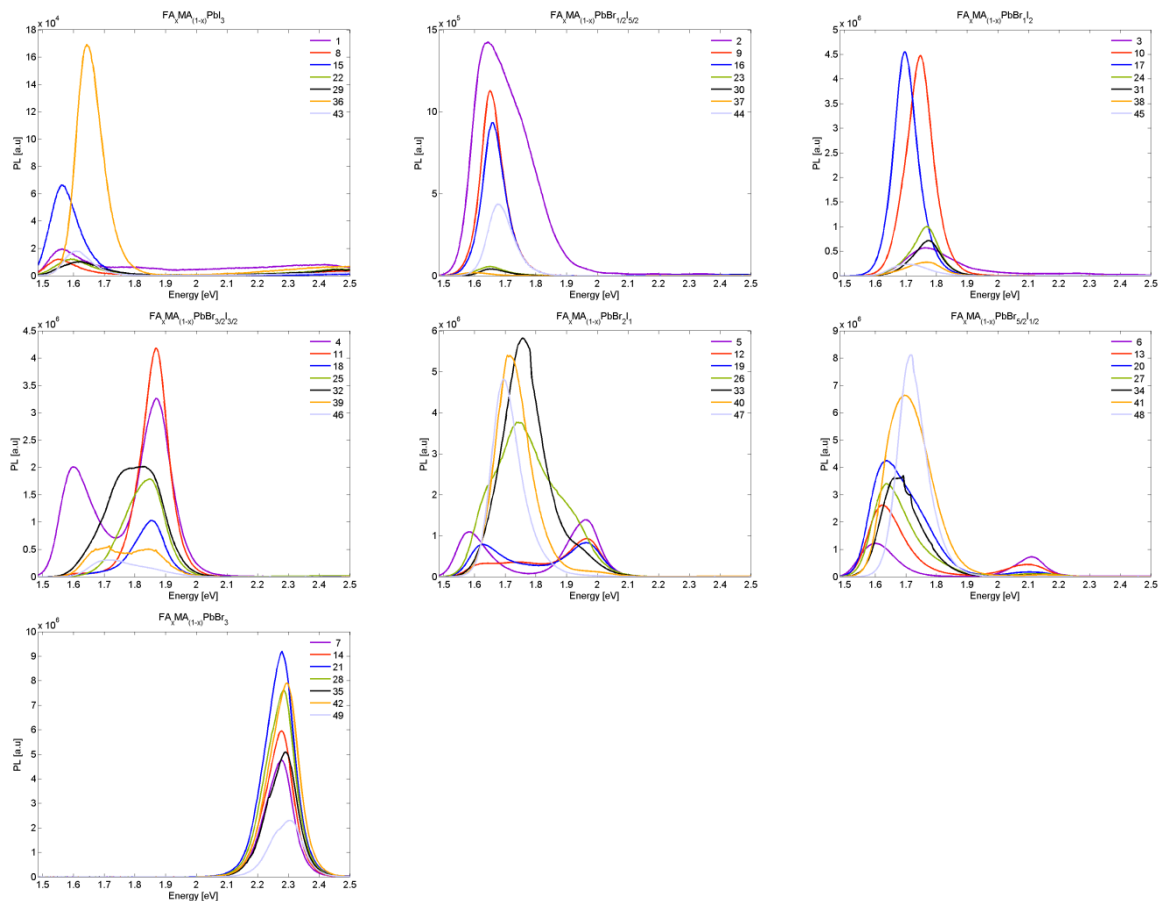


Figure S.20. Steady state photoluminescence against wavelength. Each figure represents a fixed Br/I -ration and a changing MA/FA-ration. Data is not normalized.

SEM

SEM images were of the top view of the samples were taken for all compositions. In figure S.21 Images for composition 16, which give the best working devices, with an efficiency over 20 %, are given for six different magnifications. In image S.22-27 images for all compositions are compared at different magnifications. The layouts of the samples in the figures are the same as in figure 1 in the main articles. The scale bars for figure S.22-27 are the same as the scale bars for the corresponding magnification if figure S.21

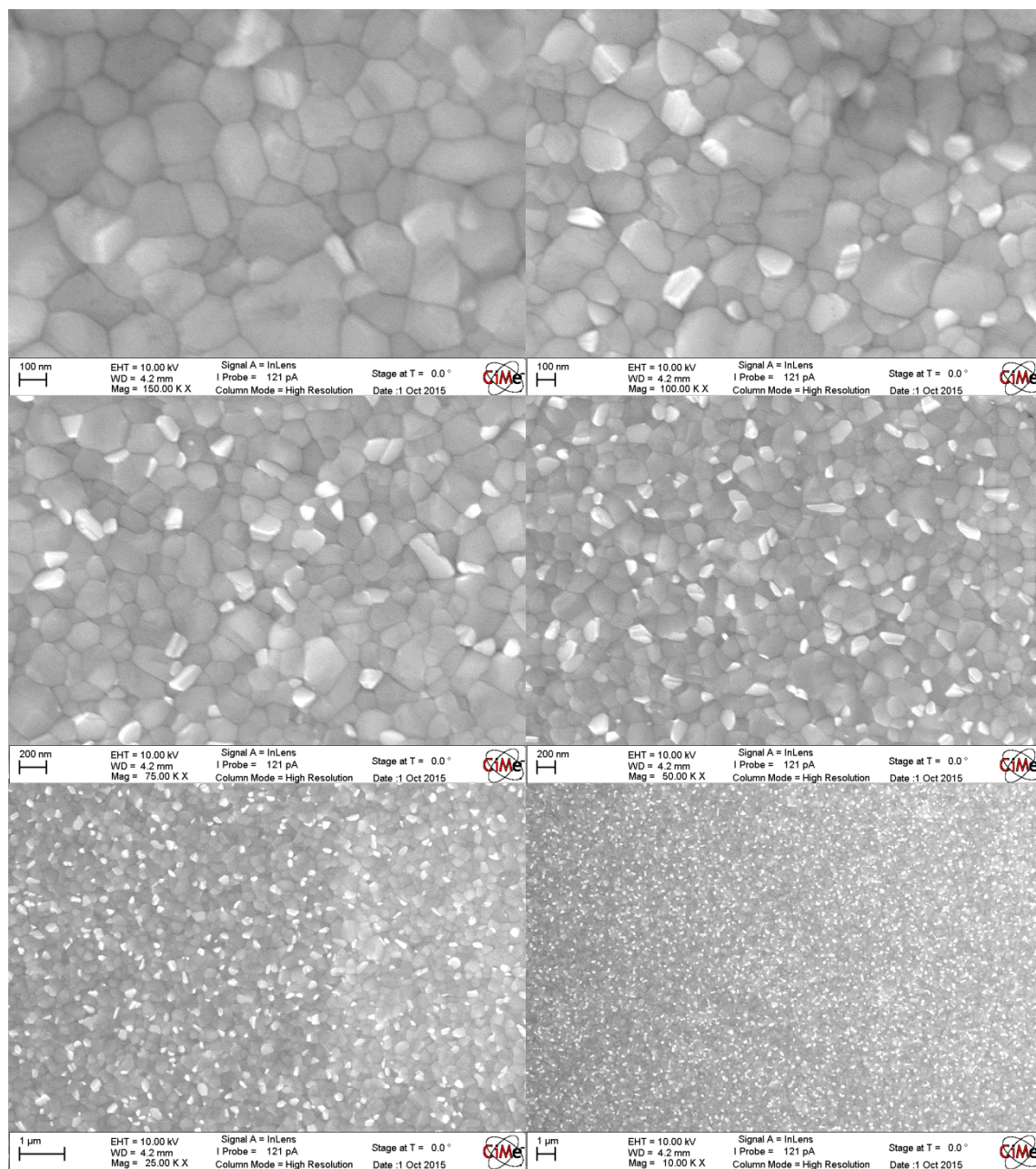
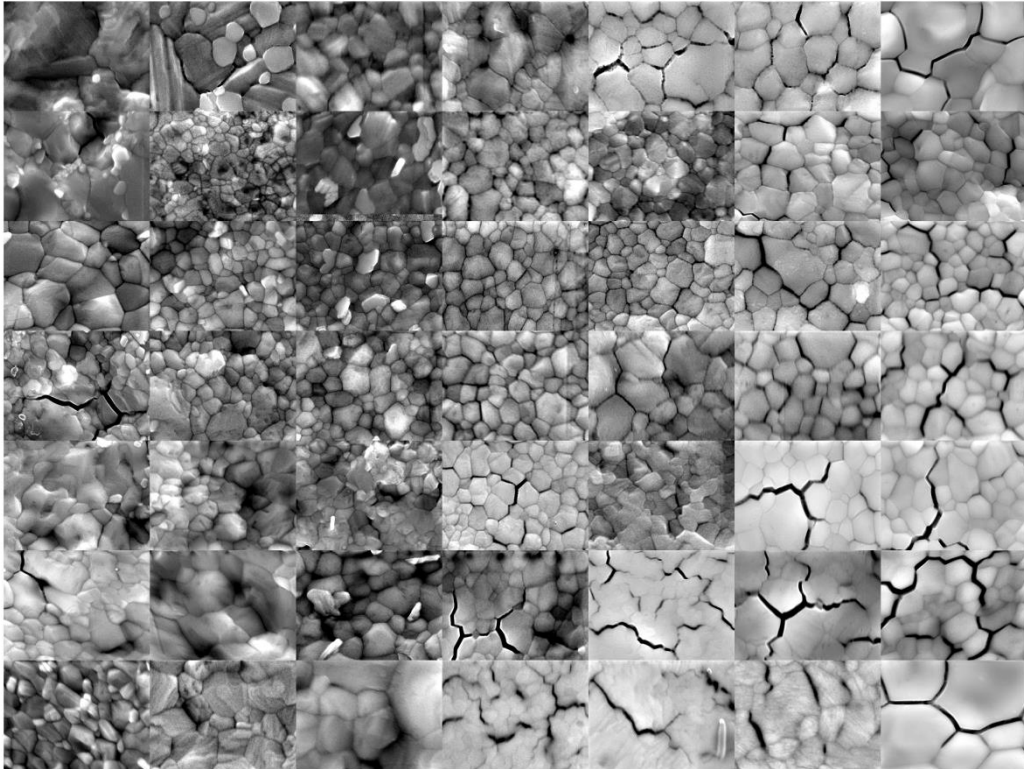


Figure S.21. SEM images of sample 16, $\text{FA}_{4/6}\text{MA}_{2/6}\text{PbBr}_{1/2}\text{I}_{5/2}$ at six different magnifications.

Magnification 150000

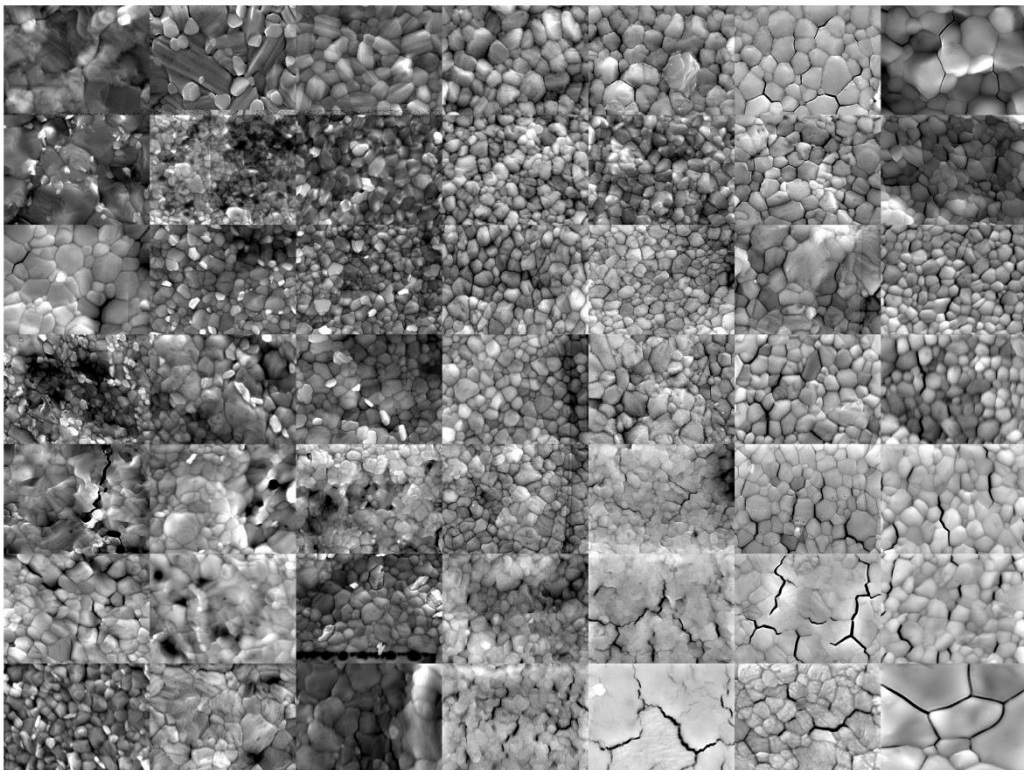
MA >>> FA



I >>> Br

Magnification 100000

MA >>> FA



I >>> Br

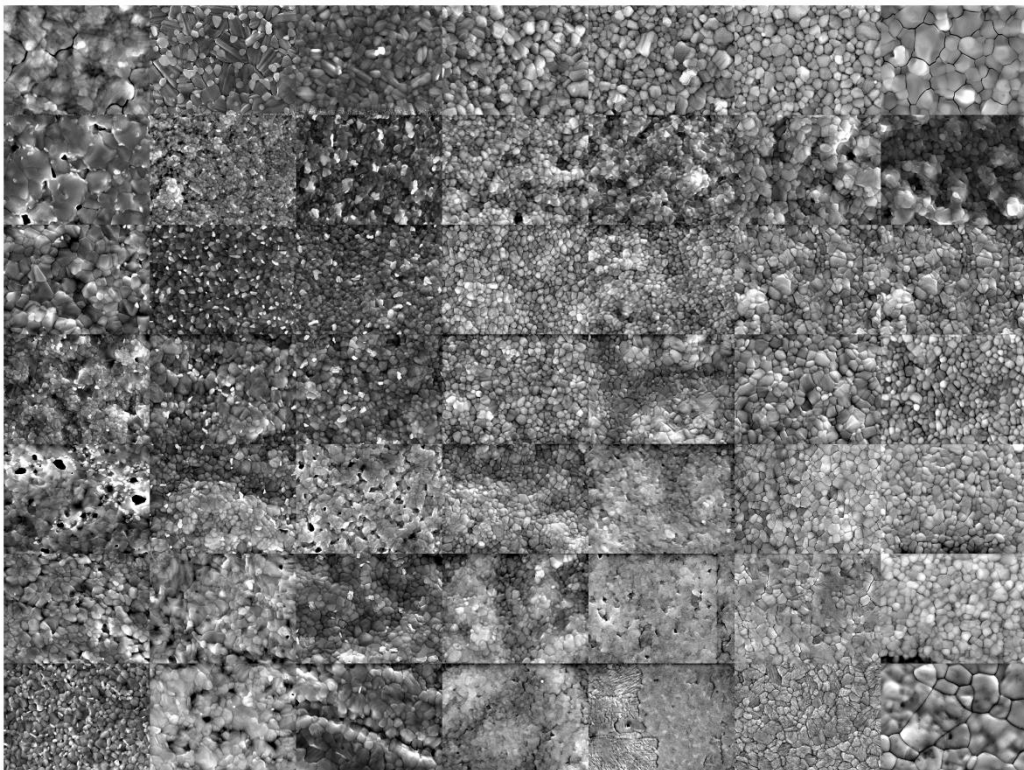
Magnification 75000

MA >>> FA



I >>> Br
Magnification 50000

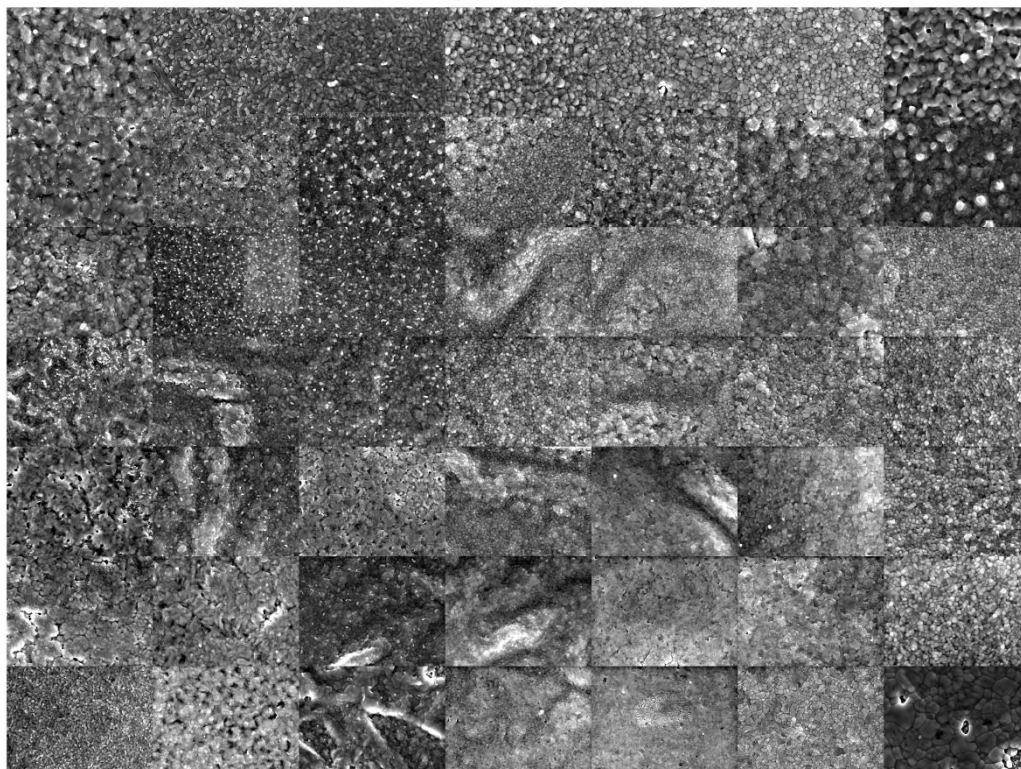
MA >>> FA



I >>> Br

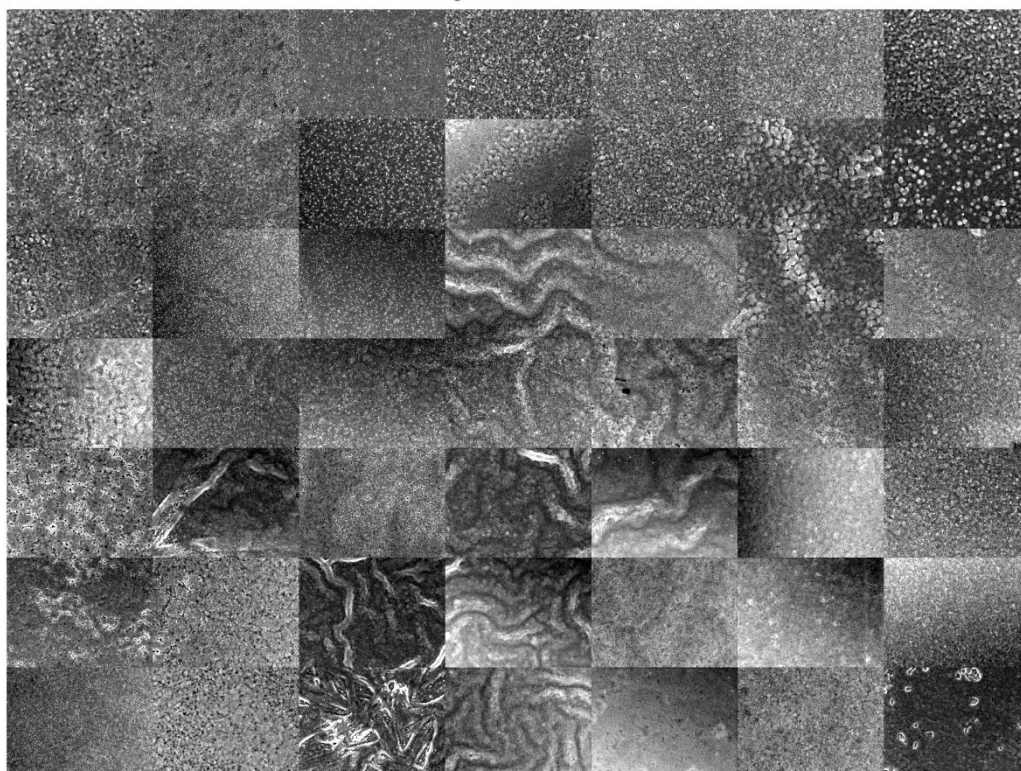
Magnification 25000

MA >>> FA



I >>> Br
Magnification 10000

MA >>> FA



I >>> Br

Image S.22-27. SEM images of all the samples at different compositions. The layout is the same as in figure 1 in the main articles. For scale bars of the individual panels se figure S.17

XRD-data

The complete set of XRD data are given in figure S.28. In figure S.29, the XRD-data is compared for samples with the same MA/FA-ratio. The seven figures in S.29 corresponds to the seven rows in figure S.28. In figure S.30 the corresponding figures for a fixed Br/I-ratio, corresponding to the columns in figure S.28, is given.

Bragg's law is stated in eqn. S.16 where λ is the wavelength, θ the diffraction angle, n the order of diffraction and d the d-spacing. The relations between the, d-spacing, the miller indices, h , k , and l , and the cell axis, a and c , is given for a cubic structure in eqn. S.17, and for a tetragonal structure in eqn. S.18. These equations were used to extract the cell parameters for the different samples, and the results are given in table S.6 under the assumption that the unit cell is cubic, and in table S.8 under the assumption that the unit cell is tetragonal. The Corresponding cell volume is given in table 4 in the main article under the assumption of a cubic unit cell, and in table S.8 under the assumption of a tetragonal unit cell.

$$n\lambda = 2d \sin \theta \quad (\text{S.16})$$

$$\frac{1}{d^2} = \frac{h^2 + k^2 + l^2}{a^2} \quad (\text{S.17})$$

$$\frac{1}{d^2} = \frac{h^2 + k^2}{a^2} + \frac{l^2}{c^2} \quad (\text{S.18})$$

Table S.6. Cell parameters. Length of a-axis determined under the assumption that the unit cell is cubic

| Pb | l_3 | $Br_{0.5}l_{2.5}$ | $Br_{1}l_2$ | $Br_{1.5}l_{1.5}$ | $Br_{2}l_1$ | $Br_{2.5}l_{0.5}$ | Br_3 |
|-------------------------------------|-------|-------------------|-------------|-------------------|-------------|-------------------|--------|
| FA | 6.34 | 6.23 | 6.22 | 6.13 | 6.08 | 6.05 | 5.99 |
| FA _{5/6} MA _{1/6} | 6.34 | 6.28 | 6.15 | 6.10 | 6.05 | 6.03 | 5.97 |
| FA _{4/6} MA _{2/6} | 6.34 | 6.27 | 6.24 | 6.10 | 6.04 | 6.00 | 5.96 |
| FA _{3/6} MA _{3/6} | 6.32 | 6.27 | 6.19 | 6.09 | 6.05 | 6.00 | 5.95 |
| FA _{2/6} MA _{4/6} | 6.31 | 6.24 | 6.18 | 6.08 | 6.04 | 6.00 | 5.94 |
| FA _{1/6} MA _{5/6} | 6.25 | 6.30 | 6.17 | 6.04 | 6.01 | 5.93 | 5.93 |
| MA | 6.28 | 6.22 | 6.16 | 6.10 | 6.05 | 6.05 | 5.93 |

Table S.7. Cell parameters. Length of a-axis determined under the assumption that the unit cell is tetragonal

| Pb | l_3 | $Br_{0.5}l_{2.5}$ | $Br_{1}l_2$ | $Br_{1.5}l_{1.5}$ | $Br_{2}l_1$ | $Br_{2.5}l_{0.5}$ | Br_3 |
|-------------------------------------|-------|-------------------|-------------|-------------------|-------------|-------------------|--------|
| FA | 8.98 | 8.58 | 8.83 | 8.92 | 8.63 | 8.55 | 8.46 |
| FA _{5/6} MA _{1/6} | 8.97 | 8.88 | 8.79 | 8.68 | 8.60 | 8.53 | 8.46 |
| FA _{4/6} MA _{2/6} | 8.95 | 8.86 | 8.83 | 8.68 | 8.58 | 8.52 | 8.44 |
| FA _{3/6} MA _{3/6} | 8.94 | 8.85 | 8.74 | 8.66 | 8.56 | 8.49 | 8.43 |
| FA _{2/6} MA _{4/6} | 8.92 | 8.82 | 8.73 | 8.64 | 8.56 | 8.48 | 8.41 |
| FA _{1/6} MA _{5/6} | 8.83 | 8.90 | 8.72 | 8.63 | 8.54 | 8.47 | 8.40 |
| MA | 8.86 | 8.79 | 8.71 | 8.62 | 8.53 | 8.46 | 8.38 |

Table S.8. Cell volume for the tetragonal unit cell under the assumption that the structure is tetragonal

| Pb | l_3 | $Br_{0.5}l_{2.5}$ | $Br_{1}l_2$ | $Br_{1.5}l_{1.5}$ | $Br_{2}l_1$ | $Br_{2.5}l_{0.5}$ | Br_3 |
|-------------------------------------|-------|-------------------|-------------|-------------------|-------------|-------------------|--------|
| FA | 12.70 | 12.89 | 12.62 | 12.44 | 12.21 | 12.09 | 11.97 |
| FA _{5/6} MA _{1/6} | 12.68 | 12.56 | 12.43 | 12.28 | 12.17 | 12.07 | 11.96 |
| FA _{4/6} MA _{2/6} | 12.66 | 12.54 | 12.48 | 12.27 | 12.11 | 12.02 | 11.94 |
| FA _{3/6} MA _{3/6} | 12.64 | 12.53 | 12.38 | 12.26 | 12.15 | 12.00 | 11.91 |
| FA _{2/6} MA _{4/6} | 12.63 | 12.47 | 12.36 | 12.23 | 12.13 | 12.00 | 11.90 |
| FA _{1/6} MA _{5/6} | 12.49 | 12.58 | 12.34 | 12.23 | 12.87 | 12.39 | 11.87 |
| MA | 12.54 | 12.44 | 12.32 | 12.20 | 12.42 | 12.38 | 11.85 |

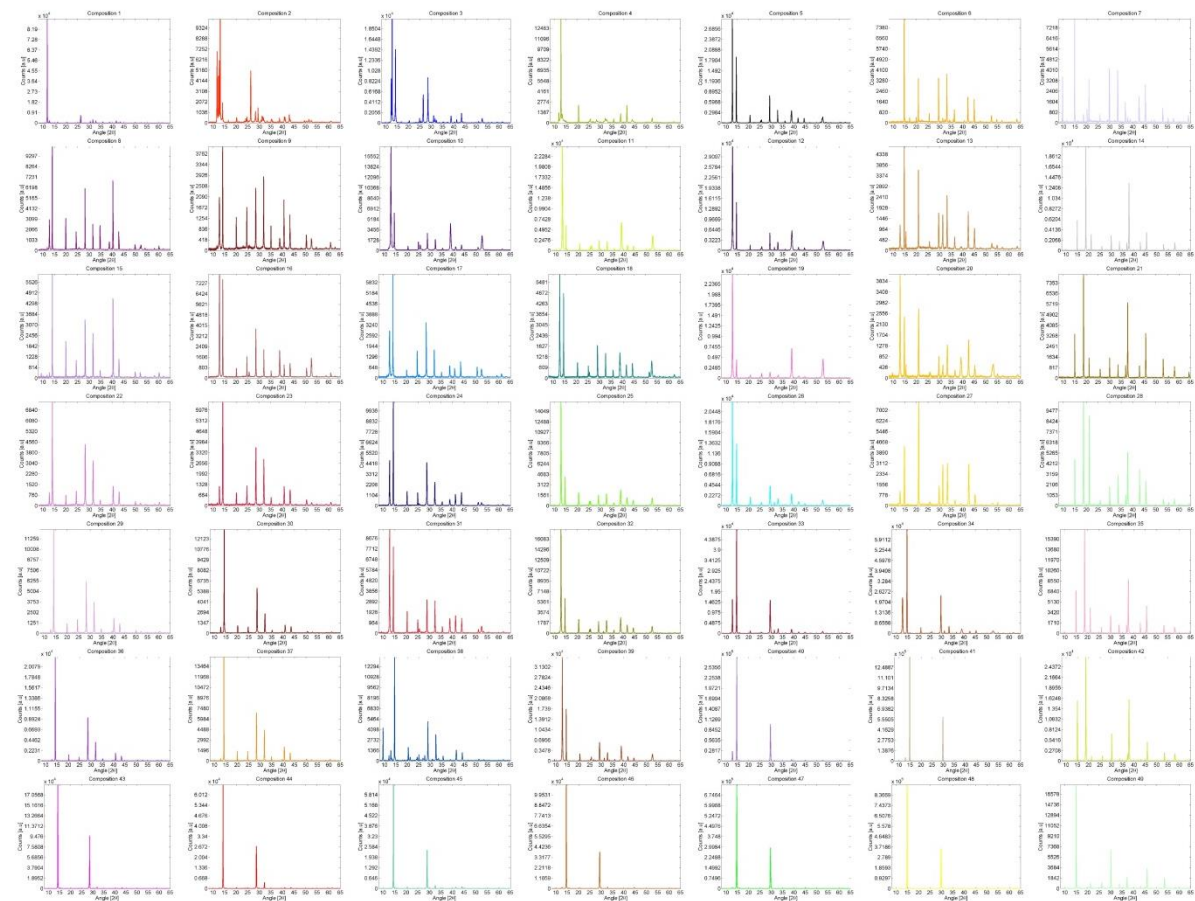
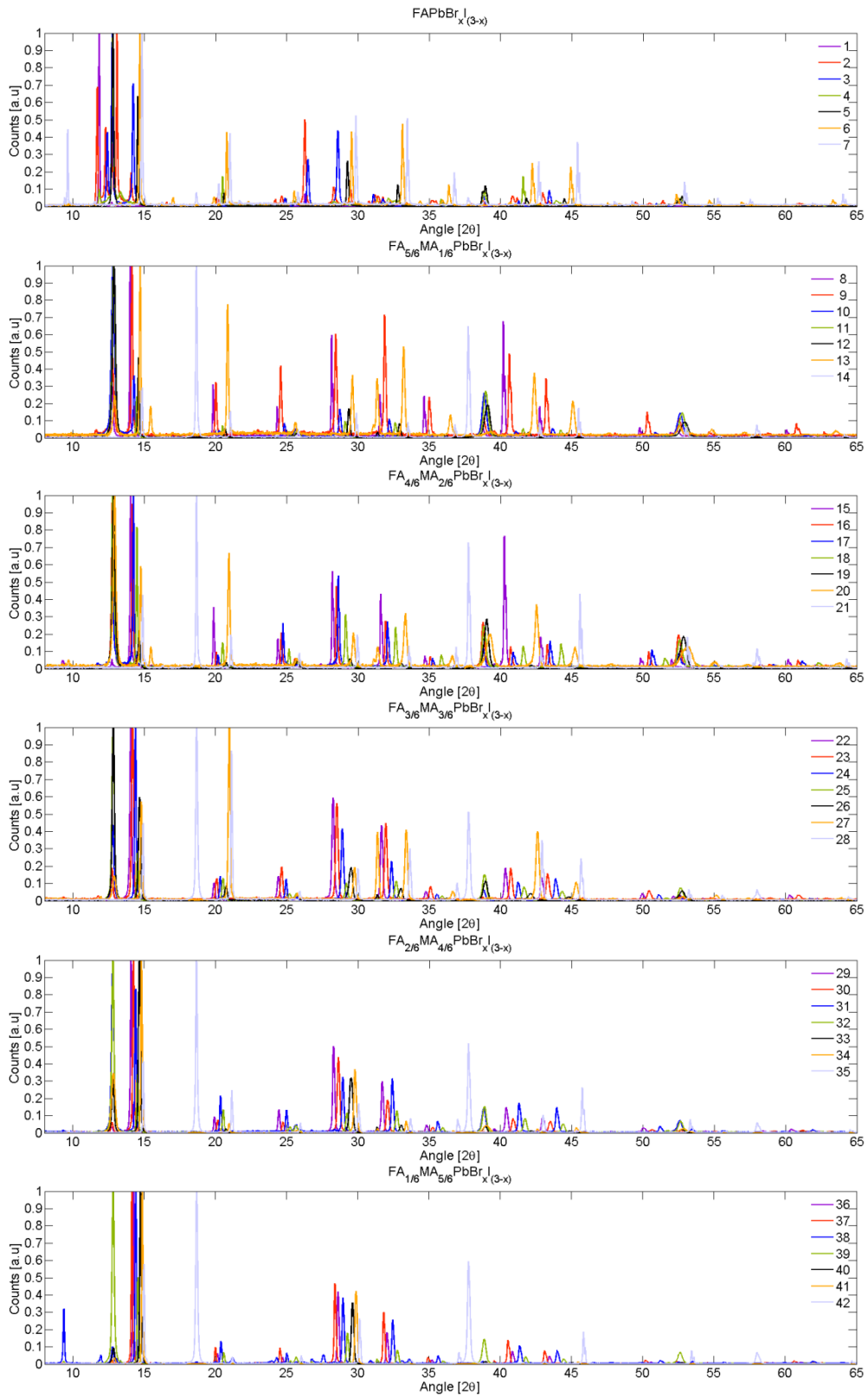


Figure S.28. XRD-data for all 49 compositions. The layout of the sub panels are the same as in figure 1 in the main article.



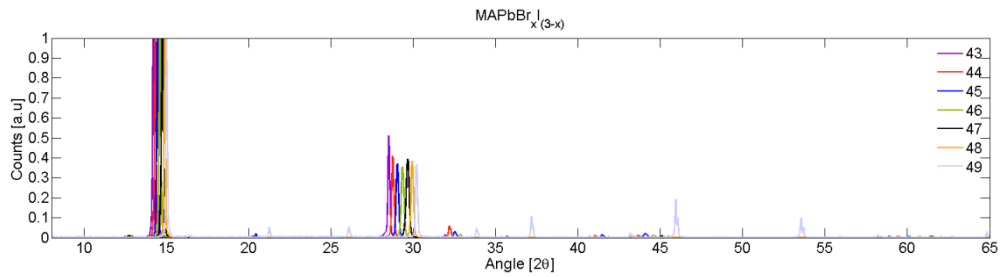
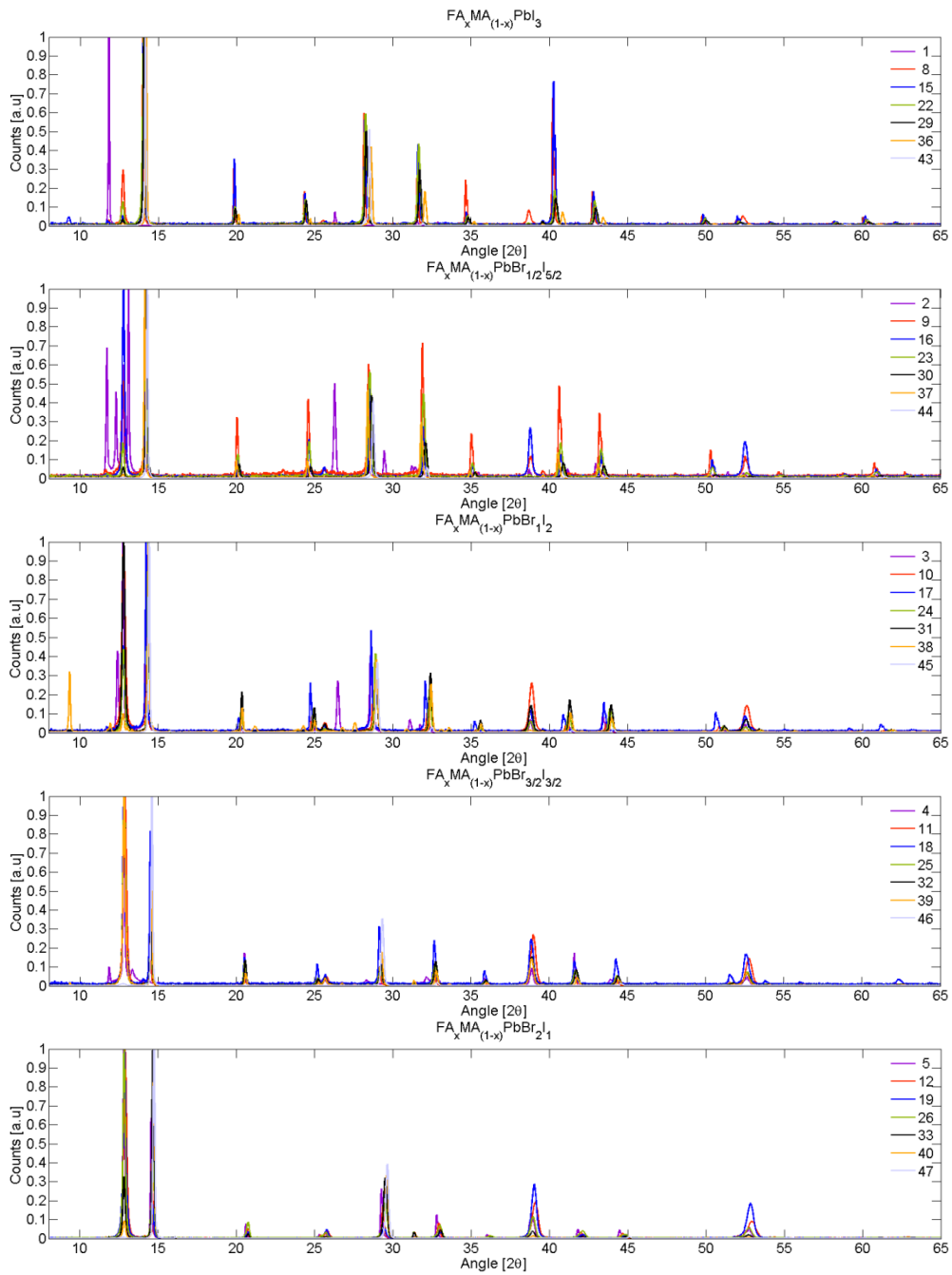


Figure S.29 XRD-data is compared for samples with the same MA/FA-ratio. The seven figure sin S.25 corresponds to the seven rows in figure S.24.



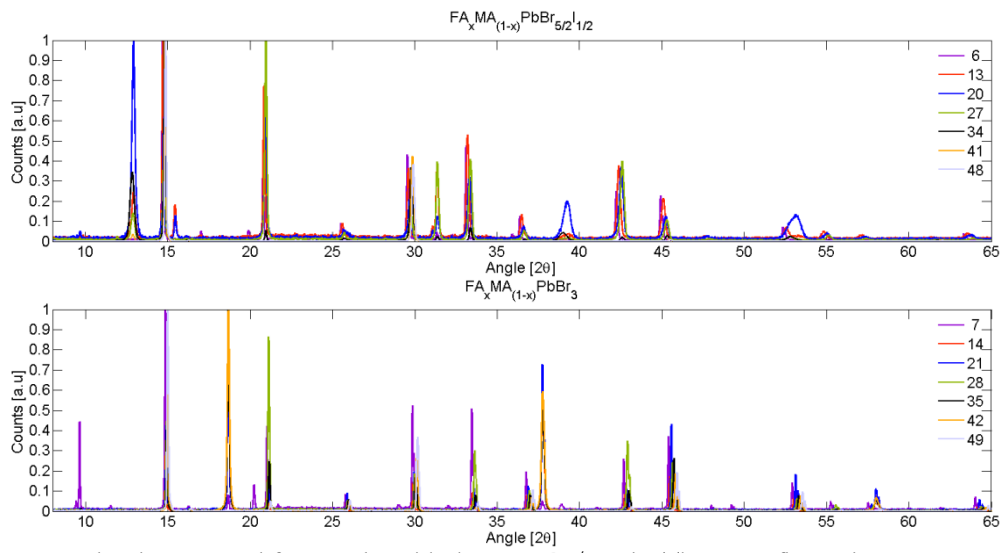


Figure S.30. XRD-data is compared for samples with the same Br/I-ratio. The seven figure sin S.26 corresponds to the seven columns in figure S.24

Device data

In figure S.31 IV-curves are given for all devices. The layout of the figures is the same as in figure 1 in the main article. In figure S.32 the device data is given in the form of bar plots seen from above.

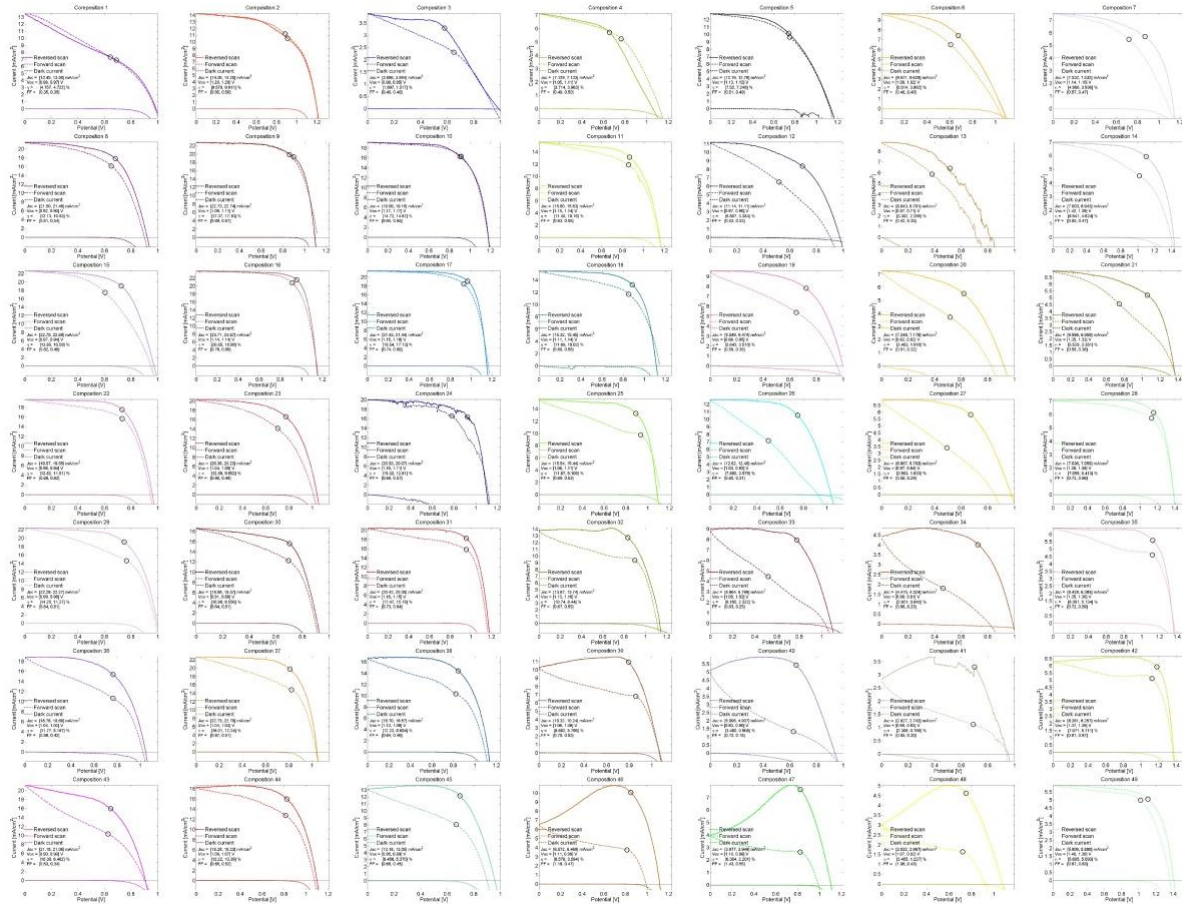
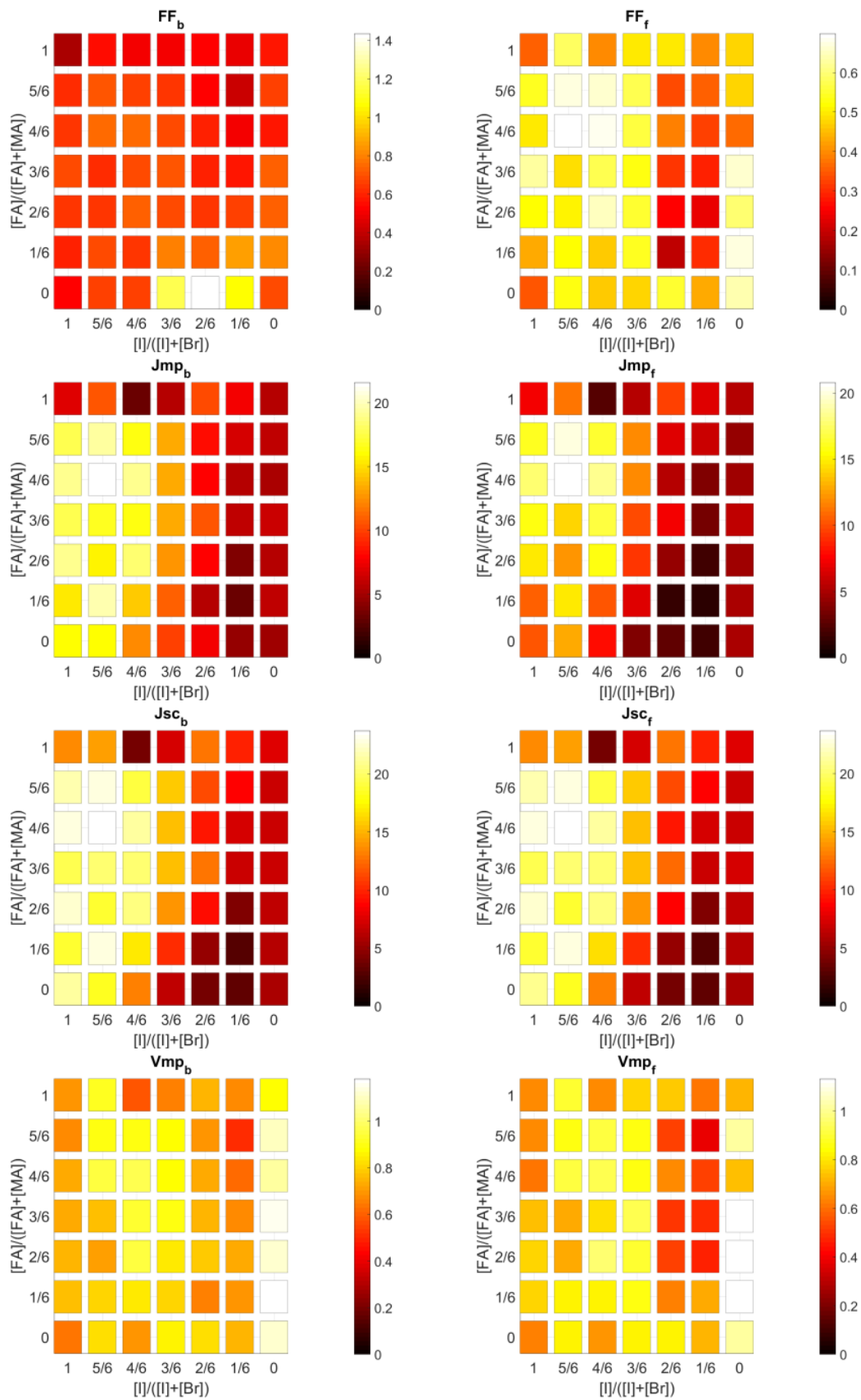


Figure S.31. IV-curves for all devices. The layout of the figures is the same as in figure 1 in the main article.



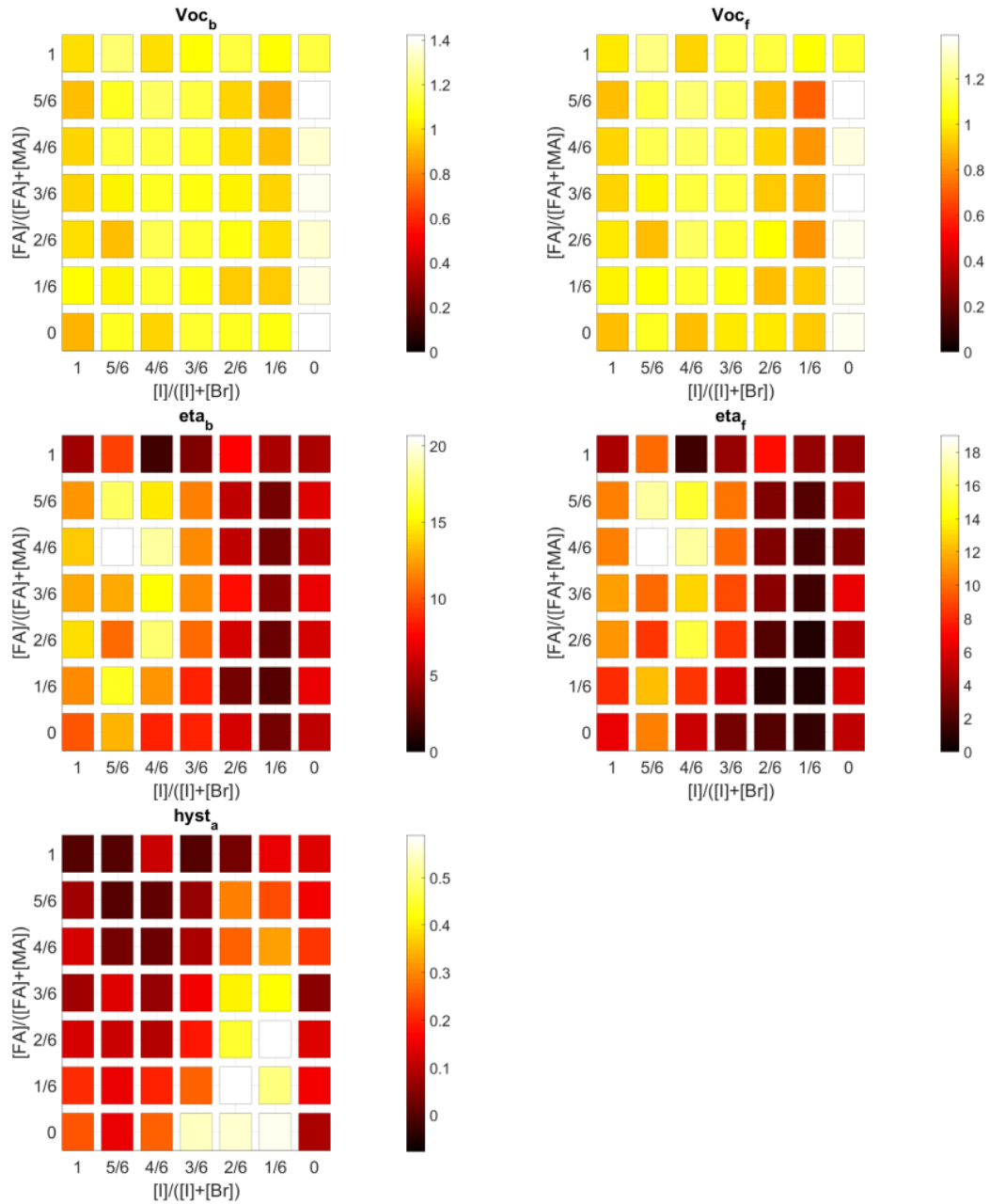


Figure S.32. Device data in the form of bar plots seen from above. b is for backwards scan and f is for forward scan. FF is the fill factor, J_{mp} is the current at the maximum current power point, J_{sc} is the short circuit current, V_{mp} is the voltage at the maximum power point, Voc is the open circuit voltage, η is the efficiency and $hyst_a$ is the hysteresis according to eqn. 3 in the main article.

References

1. Momma, K.; Izumi, F., VESTA 3 for three-dimensional visualization of crystal, volumetric and morphology data. *Journal of Applied Crystallography* **2011**, *44*, 1272-1276.
2. Goldschmidt, V. M., The laws of crystal chemistry. *Naturwissenschaften* **1926**, *14*, 477-485.
3. McKinnon, N. K.; Reeves, D. C.; Akabas, M. H., 5-HT₃ receptor ion size selectivity is a property of the transmembrane channel, not the cytoplasmic vestibule portals. *J. Gen. Physiol.* **2011**, *138*, (4), 453-466.
4. Dang, Y. Y.; Liu, Y.; Sun, Y. X.; Yuan, D. S.; Liu, X. L.; Lu, W. Q.; Liu, G. F.; Xia, H. B.; Tao, X. T., Bulk crystal growth of hybrid perovskite material CH₃NH₃PbI₃. *Crystengcomm* **2015**, *17*, (3), 665-670.
5. Dong, Q.; Fang, Y.; Shao, Y.; Mulligan, P.; Qiu, J.; Cao, L.; Huang, J., Electron-hole diffusion lengths > 175 μm in solution-grown CH₃NH₃PbI₃ single crystals. *Science* **2015**, *347*, (6225), 967-970.
6. Shi, D.; Adinolfi, V.; Comin, R.; Yuan, M.; Alarousu, E.; Buin, A.; Chen, Y.; Hoogland, S.; Rothenberger, A.; Katsiev, K.; Losovyj, Y.; Zhang, X.; Dowben, P. A.; Mohammed, O. F.; Sargent, E. H.; Bakr, O. M., Low trap-state density and long carrier diffusion in organolead trihalide perovskite single crystals. *Science* **2015**, *347*, (6221), 519-522.
7. Zhao, P.; Xu, J.; Dong, X.; Wang, L.; Ren, W.; Bian, L.; Chang, A., Large-Size CH₃NH₃PbBr₃ Single Crystal: Growth and In Situ Characterization of the Photophysics Properties. *J. Phys. Chem. Lett* **2015**, *6*, (13), 2622-2628.
8. Aygueler, M. F.; Weber, M. D.; Puscher, B. M. D.; Medina, D. D.; Docampo, P.; Costa, R. D., Light-Emitting Electrochemical Cells Based on Hybrid Lead Halide Perovskite Nanoparticles. *J. Phys. Chem. C* **2015**, *119*, (21), 12047-12054.
9. Pang, S.; Hu, H.; Zhang, J.; Lv, S.; Yu, Y.; Wei, F.; Qin, T.; Xu, H.; Liu, Z.; Cui, G., NH₂CH=NH₂PbI₃: An Alternative Organolead Iodide Perovskite Sensitizer for Mesoscopic Solar Cells. *Chem. Mater.* **2014**, *26*, (3), 1485-1491.
10. Koh, T. M.; Fu, K.; Fang, Y.; Chen, S.; Sum, T. C.; Mathews, N.; Mhaisalkar, S. G.; Boix, P. P.; Baikie, T., Formamidinium-Containing Metal-Halide: An Alternative Material for Near-IR Absorption Perovskite Solar Cells. *J. Phys. Chem. C* **2014**, *118*, (30), 16458-16462.
11. Eperon, G. E.; Stranks, S. D.; Menelaou, C.; Johnston, M. B.; Herz, L. M.; Snaith, H. J., Formamidinium lead trihalide: a broadly tunable perovskite for efficient planar heterojunction solar cells. *Energ. Environ. Sci.* **2014**, *7*, (3), 982-988.
12. Lv, S.; Pang, S.; Zhou, Y.; Padture, N. P.; Hu, H.; Wang, L.; Zhou, X.; Zhu, H.; Zhang, L.; Huang, C.; Cui, G., One-step, solution-processed formamidinium lead trihalide (FAPbI₃(1-x)Cl_x) for mesoscopic perovskite-polymer solar cells. *Phys. Chem. Chem. Phys.* **2014**, *16*, (36), 19206-19211.
13. Stoumpos, C. C.; Malliakas, C. D.; Kanatzidis, M. G., Semiconducting Tin and Lead Iodide Perovskites with Organic Cations: Phase Transitions, High Mobilities, and Near-Infrared Photoluminescent Properties. *Inorg. Chem.* **2013**, *52*, (15), 9019-9038.
14. Hanusch, F. C.; Wiesenmayer, E.; Mankel, E.; Binek, A.; Angloher, P.; Fraunhofer, C.; Giesbrecht, N.; Feckl, J. M.; Jaegermann, W.; Johrendt, D.; Bein, T.; Docampo, P., Efficient Planar Heterojunction Perovskite Solar Cells Based on Formamidinium Lead Bromide. *J. Phys. Chem. Lett* **2014**, *5*, (16), 2791-2795.
15. Jacobsson, T. J.; Schwan, L. J.; Ottosson, M.; Hagfeldt, A.; Edvinsson, T., Determination of Thermal Expansion Coefficients and Locating the Temperature-

- Induced Phase Transition in Methylammonium Lead Perovskites Using X-ray Diffraction. *Inorg. Chem.* **2015**, *54*, (22), 10678-85.
16. Jain, A.; Shyue Ping, O.; Hautier, G.; Chen, W.; Richards, W. D.; Dacek, S.; Cholia, S.; Gunter, D.; Skinner, D.; Ceder, G.; Persson, K. A., Commentary: The Materials Project: A materials genome approach to accelerating materials innovation. *Appl Materials* **2013**, *1*, (1).
 17. Chen, Q.; Zhou, H.; Hong, Z.; Luo, S.; Duan, H.-S.; Wang, H.-H.; Liu, Y.; Li, G.; Yang, Y., Planar Heterojunction Perovskite Solar Cells via Vapor-Assisted Solution Process. *JACS.* **2014**, *136*, (2), 622-625.
 18. Snaith, H. J., Perovskites: The Emergence of a New Era for Low-Cost, High-Efficiency Solar Cells. *J. Phys. Chem. Lett* **2013**, *4*, (21), 3623-3630.
 19. Bailie, C. D.; Christoforo, M. G.; Mailoa, J. P.; Bowering, A. R.; Unger, E. L.; Nguyen, W. H.; Burschka, J.; Pellet, N.; Lee, J. Z.; Graetzel, M.; Noufi, R.; Buonassisi, T.; Salleo, A.; McGehee, M. D., Semi-transparent perovskite solar cells for tandems with silicon and CIGS. *Energ. Environ. Sci.* **2015**, *8*, (3), 956-963.
 20. Filipic, M.; Loeper, P.; Niesen, B.; De Wolf, S.; Krc, J.; Ballif, C.; Topic, M., CH₃NH₃PbI₃ perovskite/silicon tandem solar cells: characterization based optical simulations. *Opt. Express* **2015**, *23*, (7), A263-A278.
 21. Bailie, C. D.; McGehee, M. D., High-efficiency tandem perovskite solar cells. *Mrs Bull.* **2015**, *40*, (8), 681-685.
 22. Shockley, W.; Queisser, H. J., Detailed Balance Limit of Efficiency of p-n Junction Solar Cells. *Journal of Applied Physics* **1961**, *32*, (3), 510-519.
 23. Weber, M. F.; Dignam, M. J., Efficiency of Splitting Water with Semiconducting Photoelectrodes. *J. Electrochem. Soc.* **1984**, *131*, (6), 1258-1265.
 24. Mosconi, E.; Amat, A.; Nazeeruddin, M. K.; Graetzel, M.; De Angelis, F., First-Principles Modeling of Mixed Halide Organometal Perovskites for Photovoltaic Applications. *J. Phys. Chem. C* **2013**, *117*, (27), 13902-13913.
 25. Umari, P.; Mosconi, E.; De Angelis, F., Relativistic GW calculations on CH₃NH₃PbI₃ and CH₃NH₃SnI₃ Perovskites for Solar Cell Applications. *Sci. Rep.* **2014**, *4*.
 26. Filip, M. R.; Eperon, G. E.; Snaith, H. J.; Giustino, F., Steric engineering of metal-halide perovskites with tunable optical band gaps. *Nat Commun* **2014**, *5*.
 27. Geng, W.; Zhang, L.; Zhang, Y.-N.; Lau, W.-M.; Liu, L.-M., First-Principles Study of Lead Iodide Perovskite Tetragonal and Orthorhombic Phases for Photovoltaics. *J. Phys. Chem. C* **2014**, *118*, (34), 19565-19571.
 28. Jacobsson, T. J.; Pazoki, M.; Hagfeldt, A.; Edvinsson, T., Goldschmidt's Rules and Strontium Replacement in Lead Halogen Perovskite Solar Cells: Theory and Preliminary Experiments on CH₃NH₃SrI₃. *J. Phys. Chem. C* **2015**.
 29. Quarti, C.; Mosconi, E.; Ball, J. M.; D'Innocenzo, V.; Tao, C.; Pathak, S.; Snaith, H. J.; Petrozza, A.; De Angelis, F., Structural and optical properties of methylammonium lead iodide across the tetragonal to cubic phase transition: implications for perovskite solar cells. *Energ. Environ. Sci.* **2016**.